UNIVERSIDADE ESTADUAL DE CAMPINAS
FACULDADE DE ENGENHARIA ELÉTRICA E DE COMPUTAÇÃO

Paloma Elias da Silva Pellegrini

Focusing in Multimode Waveguides by Wavefront Shaping

Focos em Guias de Onda Multimodo através da Modulação de Frentes de Onda

Campinas
2022

Paloma Elias da Silva Pellegrini

Focusing in Multimode Waveguides by Wavefront Shaping

Focos em Guias de Onda Multimodo através da Modulação de Frentes de Onda

Thesis presented to the Faculty of Electrical and Computing Engineering of the University of Campinas in partial fulfillment of the requirements for the degree of Doctor in Electrical Engineering, in the area of Telecommunications and Telematics.

Tese apresentada à Faculdade de Engenharia Elétrica e de Computação da Universidade Estadual de Campinas como parte dos requisitos exigidos para a obtenção do título de Doutora em Engenharia Elétrica, na Área de Telecomunicações e Telemática.

Supervisor/Orientador: Lucas Heitzmann Gabrielli

Este exemplar corresponde à versão final da tese defendida pela aluna Paloma E. S. Pellegrini, e orientada pelo Prof. Dr. Lucas Heitzmann Gabrielli.

Campinas
2022

Ficha catalográfica
Universidade Estadual de Campinas
Biblioteca da Área de Engenharia e Arquitetura
Elizangela Aparecida dos Santos Souza - CRB 8/8098

P364f

Pellegrini, Paloma Elias da Silva, 1992-
Focusing in multimode waveguides by wavefront shaping / Paloma Elias da Silva Pellegrini. – Campinas, SP : [s.n.], 2022.

Orientador: Lucas Heitzmann Gabrielli.
Tese (doutorado) – Universidade Estadual de Campinas, Faculdade de Engenharia Elétrica e de Computação.

1. Tecnologia de fibra óptica. 2. Modulação de fase. 3. Imagem óptica. 4. Análise em multi modos. 5. Acoplamentos. I. Gabrielli, Lucas Heitzmann, 1982-. II. Universidade Estadual de Campinas. Faculdade de Engenharia Elétrica e de Computação. III. Título.

Informações para Biblioteca Digital

Título em outro idioma: Focos em guias de onda multimodo através da modulação de frentes de onda
Palavras-chave em inglês:
Optical fibers
Phase modulation
Optical images
Multimode analysis
Coupling
Área de concentração: Telecomunicações e Telemática
Titulação: Doutora em Engenharia Elétrica
Banca examinadora:
Lucas Heitzmann Gabrielli [Orientador]
Jhonattan Cordoba Ramirez
Jaime Cardenas
Roberto Ricardo Panepucci
Darli Augusto de Arruda Mello e Michel Zamboni Rached
Data de defesa: 30-05-2022
Programa de Pós-Graduação: Engenharia Elétrica

Identificação e informações acadêmicas do(a) aluno(a)
- ORCID do autor: https://orcid.org/0000-0001-7848-0129
- Currículo Lattes do autor: http://lattes.cnpq.br/2233875696112340

Comissão Julgadora – Tese de Doutorado

Candidata: Paloma Elias da Silva Pellegrini **RA:** 108233

Data da defesa: 30 de Maio de 2022

Título da Tese: "Focusing in Multimode Waveguides by Wavefront Shaping"

Prof. Dr. Lucas Heitzmann Gabrielli, FEEC/UNICAMP)
Prof. Dr. Jhonattan Cordoba Ramirez (UFMG)
Prof. Dr. Jaime Cardenas (University of Rochester)
Dr. Roberto Ricardo Panepucci (Centro de Tecnologia da Informação Renato Archer/UNICAMP)
Prof. Dr. Darli Augusto de Arruda Mello (FEEC/UNICAMP)
Prof. Dr. Michel Zamboni Rached (FEEC/UNICAMP)

A Ata de Defesa, com as respectivas assinaturas dos membros da Comissão Examinadora, encontrase no SIGA/Sistema de Fluxo de Dissertação/Tese e na Secretaria de Pós-Graduação da Faculdade de Engenharia Elétrica e de Computação.

To my parents, my grandparents and my uncle, for all the support. Also, to all of those who have defended Science in Brazil, during the recent difficult times.

Acknowledgment

To begin with, I would like to express my warm gratitudes to prof. Lucas Gabrielli. Thank you for all the patience and for being there during all this work. I have learned a lot from you during these years.

I am very privileged to come from such a special family who I deeply love. I would like to thank my parents for all the effort they made to invest in my education. My father has played a major role in my life by instigating my creativity and participating in every way he could, while my mother has always surrounded me with unconditional love and comfort. I would also like to thank my grandparents for taking such good care of our family. I feel very lucky to have, at home, my mother and my grandmother as examples of strong and powerful women. And, of course, I would like to thank my uncle for being so close to me. He was the first person to talk about Physics to me, he was the one who expanded my horizons and showed me how much we still have to know.

I would like to give thanks to everybody from LEMAC, LCON and CTI for all the fruitful conversation. Especially, a heartfelt thank you to Paulo Jarshel, Julian Pita and Claudecir Biazoli for all the help they gave me during this work.

These years would definitely be harder without my dear friends. The ones that made this journey so joyful and much more fun. I have also learned a lot from them. Thanks to my friends who were partners in so many trips, hikes and climbs, the ones who faced a pandemics with me and those that were always there, for the better and for the worse. Thanks for being with me everyday, for being my support in the difficult times and for all the good laughter that we have shared. You have made all the difference.

Finally, I am very grateful for every teacher that I have ever had. I appreciate all the people that accounted for my education and all the ones that played part in the well functioning of the university.

Also, I would like to acknowledge the financial aid received by CNPQ, with grant 168970/2018-0.

Without the possibility of error and real indeterminacy implied by the quantum theory, human liberty is meaningless.
Heinz R. Pagels, The Cosmic Code: Quantum Physics as the Language of Nature

Resumo

Este trabalho tem como objetivo demonstrar como gerar foco com fibras ópticas multimodo através da modulação de fase das frentes de onda. Para realizar os experimentos de imageamento, em 633 nm, um modulador espacial de fase foi codificado para modular as frentes de onda do feixe incidente com máscaras de fase. Então, ao fazer a aquisição do padrão de espalhamento na saída da fibra óptica, uma relaçao entre fase e magnitude foi estabelecida e a matriz de transmissão das fibras foi calculada.

A montagem experimental proposta, neste trabalho, é relativamente simples. Ela é mecanicamente estável e não requer nenhum feixe de referência, assim, utilizando as matrizes de transmissão calculadas, pontos focais podem ser gerados na saída da fibra.

Este experimento de imageamento pode ser aplicado em diversas áreas, como bio imageamento e sistemas integrados. Para explorar essas possibilidades, experimento de acoplamento foram realizados. Acoplamentos fibra-fibra e fibra-chip foram estudados e mostramos que a potência de saída teve ganhos de até 4.5 db quando comparada com a montagem sem a máscara de fase utilizada. Os experimentos propostos são vantajosos por eliminar a etapa - comum - de fabricação de lentes na ponta de fibras ópticas para configurações de acoplamento. Além disso, essa montagem proposta não requer monitoramento da saída da fibra.

Abstract

This work aims to demonstrate focusing with multimode optical fibers by phase wavefront shaping. To perform imaging at 633 nm, a phase-only spatial light modulator (SLM) was coded in order to shape the wavefronts of the input beam by using phase masks. Then, by the output speckle from the multimode optical fiber a relation between phase and magnitude was established and the transmission matrices of the fibers were retrieved.

The experimental setup proposed, in this work, is relatively simple - it is mechanically stable and does not require any additional reference beam - thus, by using the retrieved transmission matrices, focusing could be achieved at the distal end of the fiber. Such imaging experiment opens up multiple application in bio-imaging and integrated systems.

To explore these promising possibilities, coupling experiments using multimode fibers were developed. Fiber-to-fiber and fiber-to-chip coupling were experimented and we show that the output power enhanced in, approximately, 4.5 db when comparing to the configuration without the optimized phase mask. The experiments are advantageous to coupling systems once it eliminates the commonly additional fabrication of lenses at the tip of fibers, as it is not necessary to monitor the distal end of the fiber.

List of Figures

List of Tables

List of Abbreviations

SLM	spatial light modulator
TM	transmission matrix
LC	liquid crystal
BE	beam expander
P	polarizer
MMF	multimode fiber
MCF	multicore fiber
CCD	charge-coupled device
FE	factor of enhancement
OC	optical contrast
NA	numerical aperture
LUT	lookup table

Summary

Chapter 1

Introduction

Since the beginning of the 1970's, there has been an urge to comprehend information on complex media. Nowadays, the motivation lies on numerous scientific fields such as imaging in scattering media for biological applications [2,3], optical communication [4] and also optical fiber systems [5] with imaging [6,7] and coupling in integrated photonics [8] purposes. In this work, we aim to characterize modal dispersion in multimode optical fibers in order to achieve focusing with a simple experimental setup that can be applied in several imaging experiments and also can be used to enhance integrated setups.

That being said, proper techniques to control modes in such media were, initially, researched. Then, a advantageous method was studied and applied in a simple imaging experiment with different types of multimode fibers.

1.1 Wavefront Shaping

About three decades ago, the phase shifting method proved to be a useful technique to obtain phase information about the wave propagation in complex media. In an interferometric configuration, the wavefront was submitted to four different phase shifts and its reconstructed intensity gave place to modulation analyses and several optical sensing applications without the need to locate fringes, this procedure is called the Four Step Algorithm [9].

Each mentioned phase shift is a 90° step and the introduction of these shifts in the setup was commonly done by applying discrete voltages in translational mirrors coupled to piezoelectric transducers. Therefore, four intensity interference patterns could be recorded, and by mathematically manipulating their respective equations, the wavefront phase could be retrieved. The interferometric configuration brings a series of advantages such as insensitivity to spatial variations of intensity and a fixed pattern noise.

In 1980's, notions of a correlation function between the transmission and reflection coefficients were introduced [10]. Such correlation composes scattering information of the medium and will be comprehended as a transmission matrix. The study of propagating

modes in disordered systems led to interesting results of weak and strong localization that arose from these matrices. Coherence effects in diffusive regime and diffusion properties are some of its impacting conclusions, under the constrains of flux conservation and time-reversal invariance.

Statistical researches about transmission matrices provided deeper manipulation comprehension and several methodologies came up [11]. Unitarity, reciprocity and time reversal symmetry were properties worth exploring; the relations found derived from energy conservation and opened up the possibility of wave equations inversion which led to broad applications in imaging, acoustics and telecommunication [12, 13].

In the early 2000's, Popoff *et al.* proposed a method based on a TM to unambiguously reconstruct different shapes within the analyzed turbid medium [14, 15]. It was a breakthrough on the topic, once it utilized the technology of a spatial light modulator to finely sweep the phase distributions and it allowed to establish a relation between the observed amplitudes, that were collected with a photodetector, and the source. The experiment done consisted on an object, subject to a laser beam and its speckle pattern was recorded. This collected image is actually the result of multiple scattering optical channels and the technique proposed is to reconstruct the image by measuring the transmission matrix, thus it is an inverse problem.

Using phase shifting interferometry, a large number of input wavefronts were modulated with a spatial light modulator. For each one, their respective speckle is acquired. The relation between input and output is established with an operator, which is defined in [16] as the product between the reference signal (static speckle) and the transmission matrix. The latter is found by inversion. In this method, it may be necessary to use a mean square optimized operator to minimize transmission errors.

The quality of imaging reconstruction can be discussed by looking at the singular values of the transmission matrix. By increasing the number of output modes, the minimum singular value also increases. This results in choosing the output channel that transports more energy through that medium thus the more efficient operator. This singular values distribution also indicates if the propagation follows a multiple scattering regime, which is the initial hypothesis.

Although the mentioned method has been proved efficient, the inversion problem involves an interferometric configuration and the operators only have a valid performance in opaque samples in the scattering regime. Hence, the reasoning may not follow for any sample, as the ones with thickness in many orders of magnitude of their free mean path and multimode waveguides.

Thus, focusing techniques and coherent transmission in scattered and opaque media, object identification and light control in multimode waveguides became a reality and demands for different and improved techniques took place [17–19].

This subject arises other interests and a myriad of applications among them

micromanipulation [20], optical clearing [21] and optical tweezers [22]. Also multimode imaging brings direct applicabilities to the biological field, like endoscopes composed of a single MMF or either a bundle of them which offers more independent channels to the the imaging system [23, 24].

Keeping these applications in mind, the experimental setup, in here, proposed does not account for any interferometric measurements so it can be feasible for imaging with multimode fibers. So, this work initially focuses on exploring a suitable method based on quadratic optimization [14, 25]. By obtaining transmission matrices, multimode waveguides can be characterized and modal dispersion controlled through imaging, only using amplitude experimental measurements.

1.2 Focusing and Coupling Experiments with Multimode Waveguides

Multimode waveguides were once considered unreliable because of the output speckled patterns. However, the amount of propagating modes that are possible in a multimode waveguide actually translates in a great freedom to shape multiple channels, independently. Combining the multimode propagation with the cylindrical symmetry of fibers, advances in imaging, telecommunication, and many other areas have been noted [26].

It should be emphasized that the increasing demand for information transmission has motivated the research of using multimode fibers for mode division multiplexing. By using and controlling different mode shapes, they can be responsible for independent information transmissions and thus, significantly increase the amount of carried data. In free space optics and communication, mode division multiplexing brings scalable transmission capacity and spectral efficiency, for chip-to-chip configuration, the faster processing in comparison to electrical circuits also stands out [27, 28].

Although mode division multiplexing has been reported decades ago [29], some challenges still remain. Among them: maintaining alignment in free space, mode deterioration within fibers, and general implementation in integrated circuits [27].

As for imaging, the multiple modes available can provide high quality resolution [30]. Also, by using multimode fibers, it is possible to miniaturize the whole imaging system and expand the laser sources to those that do not present a high spectral purity [19].

The advantages brought by multimode fibers have propelled developments in endoscopy [31], fiber lasers [32], object recognition [33], sensing [34], microscopy [35] tomography, *in-vivo* imaging [36] and many others.

As multimode fibers have been studied as promising tools to increase resolution in microscopy and generate focus [30, 37], these fibers were used for the initial experiments, in this work, in the visible range of the spectrum. By characterizing the fibers according

to their transmission matrices, focusing was explored in a multi mode configuration.

The application of imaging with multimode fibers in endoscopy areas is also very strong nowadays. By using fiber endoscopes or even fiber bundles, progress has been made in making devices that provides three dimension imaging [38], smaller cross section, which minimizes invasion without impairing image qualitys [39], besides, multimode fiber endoscopes can be applied for imaging and illumination simultaneously [40]. The advantages of applying fiber endoscopes are numerous and varied. They are direct consequences of profiting on the multimode regime, which improves resolutions comparing to single mode as the latter suffer from near diffraction limit in resolution [41].

Moreover, multicore fibers can bring advantages when compared to the fiber bundle because their cores are well positioned whereas the cores in the bundles are disordered. Also, each core from can support multimode propagation [31]. Multicore fibers are also useful tools in bio imaging, telecommunication, coupling applications [42–44], among others. However, in the visible spectrum, their core diameters are typically too small to achieve in a single mode regime [45]. Here, we show that it is possible to work with multimode multicore fibers, so the restrain of small diameters can be relaxed.

Graded index (GRIN) fibers are also appealing waveguides in several fields. They have been extensively studied due to the their light propagation that can be suitable for communication systems, spatial and mode division multiplexing [46] and even for the study of non linear phenomena such as soliton formation [47] and self imaging [48].

Due to their parabolic refractive index profile, GRIN fibers have been promising tools when it comes to imaging as they exhibit periodic constructive interference that can maintain radial symmetry of inputs fields [49]. Recently, it has been reported may advances using these fibers. Such as in microendoscopy using GRIN lens array [38], in optical coherence tomography using a conical GRIN fiber tip [50] and in several other bio imaging applications [51, 52].

Focusing with lensed GRIN fibers is not a recent field of research [53], however it has been greatly evolving.

A series of lensed fibers, among other small probes have been developed for imaging purposes [54]. The lenses on the fibers enables focusing by tuning the divergence beam angle, the spot size and also the focal length [55, 56]. Recently, small probes of GRIN lenses were used integrated circuits in order to study neural connections and brain function *in vivo* [57].

By exploring different designs of geometries at the tip of the fibers [58], proper focus can be obtained so free-space interfacing can be improved as the necessity of bulk optics decrease. Lensed fibers can also be used in attenuators, optical cross-connect switches, as well as in collimators and couplers in free-space and integrated experiments [59–61]. Besides those, lensed fibers are also important tools in promoting efficient coupling in integrated systems [62].

However, even for different types of fibers, such as large core multimode, multicore fibers and GRIN fibers, most of the literature present studies that work in near infrared or infrared frequencies to avoid the modal mixing that comes along.

So, we can infer that the main drawback that multimode fibers bring is the unpredictable modal interference [16, 63]. Therefore, solutions to demix modes have been extensively studied and this problem mimics the unscrambling of information in complex media, earlier discussed [14, 15, 64].

Some other challenges concerning the application of multimode fibers are physical deformations of the waveguide, like bending and distance from the focal plane [19].

The transmission matrix method to characterize modal dispersion of multimode waveguides has been proved efficient in fiber systems [65, 66]. Although, when empirically measured, these challenges may involve complete new calculations of the transmission matrices, which are usually time exhausting. In these cases, methods based on machine learning can bring out better results [41].

The method, detailed in this work, can satisfactory deal with modal mixing, in a simple and stable configuration. Besides, the experiments can be performed in the visible range of the spectrum, which broadens the possibilities of applications even more.

Then, several multimode fibers were explored in this work, in focusing experiments. Large core fibers were the first waveguides used, followed by fiber bundles and also GRIN fibers. By promoting focus with the GRIN fibers without requiring fabrication of lenses, it is possible to simplify the applications aforementioned.

Still, we demonstrate how focusing with GRIN fibers, without additional lenses, can enhance two different coupling configurations for integrated systems, those being fiber-to-fiber and fiber-to-chip.

1.3 Thesis Contributions

This work targets contributions in a major field in Science, which is imaging with multimode fibers. For now, the imaging resolution aims tens of micro meters. Within this field, the challenge of dealing with modal mixing is deeply analyzed.

By applying an optimization method which requires only magnitude information from experimental data, focusing can be stably generated at the output of the waveguides once their wavefronts are shaped.

It is a simple setup that aims convenience, stability and the possibility to easily tune characteristics the focal spots, such as their diameter and operating wavelength.

Besides, this work also seeks applications in integrated systems. To address the need for satisfactory coupling efficiency, lensed fibers are usually a solution [67]. However, they do impose fabrication steps that makes coupling more complex. We propose, here, coupling without lensed fibers. We use a commercial GRIN fiber as the input waveguide

and generate focus with the studied method to enhance the out optical power in two different coupling configurations: fiber-to-fiber and fiber-to-chip.

1.4 Thesis Organization

This thesis is organized as follows:

In Chapter 2, Section 2.1 presents the multimode fibers used in this work as well as discusses their modal dispersion. The method responsible for generating focus is detailed in Section 2.1. It is also explained how the technique studied is a viable solution to characterize their modal distribution and how it is applied in the experimental setup proposed.

Chapter 3 reports focusing experiments for a multimode fiber, a multicore fiber and a fiber bundle. The focus quality is examined in this chapter, along with the resolution for imaging.

In Chapter 4, the GRIN fiber are studied aiming coupling experiments. So, in 4.1, initially, focal spots are generated using a GRIN fiber. Then, the coupling experiments for fiber-to-fiber and fiber-to-chip configurations were studied, according to their coupling efficiency in sections 4.2 and 4.3, respectively.

In Chapter 5, the overall conclusions of this work are listed.

Chapter 2

Methodology

In order to explore focusing with different multimode waveguides, it is necessary to establish a reliable method to compensate the mode mixing that comes along. In this work, we aim a robust and simple technique that provides us enough stability so there is no need to monitor the distal end of the waveguide throughout the whole experiment. Besides, the simple experimental setup to be proposed requires no reference beam. By freeing the distal end and not using interferometric measurements, the focus obtained at the tip of the waveguide can be used for a myriad of applications, including bio-imaging and integrated systems.

With these goals in mind, the method chosen relies on the retrieval of the transmission matrix of the waveguide by phase shaping the wavefronts using an SLM.

The chapter that follows details multimode fibers, in Section 2.1 and the method that applied to compensate modal mixing in Section 2.2.

2.1 Multimode Propagation in Optical Fibers

Multimode propagation is the key concept supporting this work. Therefore, based on [1, 68], a brief description, of the optical fibers here used, step index and GRIN fibers, is presented. Figure 2.1, from [1], illustrates the cross section and the refractive index profile from both fibers. The main difference between these fiber is that the refractive index of the step index fiber has a well defined and abrupt change from cladding to core, while the GRIN has a more gradual interface, its refractive index progressively decreases from cladding to core.

2.1.1 Step-Index Fiber

The refractive index profile of step index fiber with core of radius a presents well defined regions. Equation 2.1 shows the refractive index according to the propagation distance ρ. The refractive indexes of the core and cladding are n_1 and n_2, respectively.

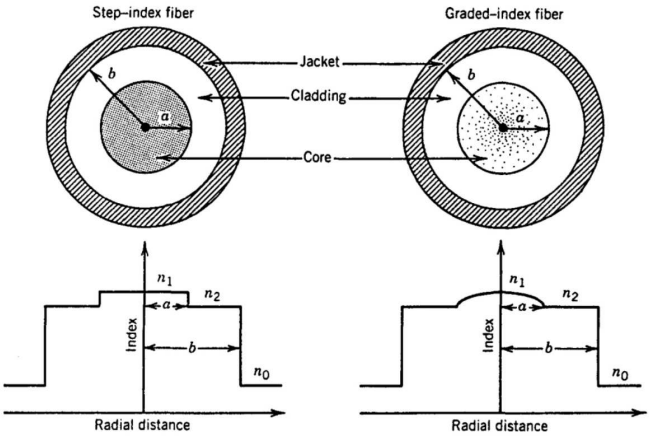

Figure 2.1: Cross section and refractive index profile for a step index (on the left) and graded index (on the right), from [1].

$$n_\rho = \begin{cases} n_1 & \rho \leq a \\ n_2 & \rho > a \end{cases} \tag{2.1}$$

It is known that propagation in optical fibers follows total internal reflection between the core and cladding media. So, only incidence angles larger than the critical angle are considered.

Taking the incidence angle as θ_i, the refractive index of the external media, the classing and the core, respectively as n_0, n_1 and n_2, we can see the following profile:

$$n_0 sin\theta_i = (n_1^2 - n_2^2)^{0.5} \tag{2.2}$$

The term on the left of Equation 2.2 is the numerical aperture of the fiber and it indicates the fiber's capability to gather light. By approximating n_1 to n_2, the numerical aperture (NA) can be reduced to:

$$NA = n_1(2\Delta)^{0.5} \tag{2.3}$$

Where $\Delta = \frac{n_1 - n_2}{n_1}$.

Aiming larger capabilities, the intermodal dispersion arises and this is the main issue dealt, in this work. It can be understood as multiple rays propagating in different paths, with different lengths.

It also worth emphasizing, in Equation 2.4, the relation between the fiber's capacity to transmit information B, in bits, over a length L, with their refractive indexes.

$$BL < \frac{n_2 c}{n_1^2 \Delta} \tag{2.4}$$

2.1.2 Graded Index Fibers

Analysing the refractive index profile for GRIN fibers, it possible to conclude that the intermodal dispersion is minimized in this fiber.

The non constant refractive index of the core of a GRIN fiber is shown in equation 2.5, where n_1 corresponds to its maximum value at the core and n_2, its minimum at the cladding interface. The core radius is a and α is the parameter that represents the profile. For a parabolic index, $\alpha = 2$.

$$n_\rho = \begin{cases} n_1[1 - \Delta(\rho/a)^\alpha] & \rho < a \\ n_1(1 - \Delta) = n_2 & \rho = a \end{cases} \tag{2.5}$$

Because of the non constant refractive index profile, the velocity of the rays in the fiber changes over the propagating length, for example, where the index is larger, rays will be slower. It means that it is feasible that all rays overlap at the end of the fiber, that is why dispersion in this fiber is reduced when compared to the step index fiber.

The information transmission for graded index fiber can be analyzed in Equation 2.6. When comparing the latter with Equation 2.4, it is seen that transmission in GRIN fibers improves approximately three times.

$$BL < \frac{8c}{n_1^2 \Delta} \tag{2.6}$$

2.1.3 Fiber Modes

To clarify the meaning of the fiber modes, the wave equation for the electric field is presented in equation 2.7, for frequencies ω and free space number k_0^2

$$\nabla^2 \mathbf{E} + n^2(\omega) k_0^2 \mathbf{E} = 0 \tag{2.7}$$

This equation can be solved in cylindrical coordinates due to the optical fiber's symmetry, where only two components are independent. Each solution obtained is comprehended as an optical mode. Note that the equation depend on the refractive index, so the solutions for the step index and GRIN fibers are different.

For the step index fiber, the solutions for the core and cladding follow eigenvalue equations of Bessel functions and an integer number m of solutions is possible, once the field is periodic. Usually, the solution can found numerically and it determines the propagation constant $\beta_{m,n}$. Each value found refers to a mode.

As electric and magnetic fields should be considered, the modes of an optical fiber are said to be hybrid.

The number of modes allowed in an optical fiber is evaluated according to the cutoff condition, by the parameter V.

For the step index fiber, the cutoff condition is shown in Equation 2.8. The total number of modes can be approximated to $V/2$.

As for the GRIN fiber, the total amount of propagating modes, N, can be found in Equation 2.9.

$$V = k_0 a (n_1^2 - n_2^2)^{0.5} \tag{2.8}$$

$$N = \frac{\alpha}{\alpha + 2} k^2 n_1^2 \Delta a^2 \tag{2.9}$$

We can then, consider a situation where there are multiple incoming modes into a fiber and, according to the fiber's characteristics, multiple others will exist on the output.

In this case, the fiber establishes a connection between input and output, by shuffling the incoming modes and returning multiple dispersed modes. Hence, there is a transmission matrix that operates in the incoming fields and generates a speckle at the output.

In this work, we aim to characterize the multimode fibers according to their transmission matrix, so the speckle, that results from modal dispersion, can be reversed.

As the amount of modes supported by the fiber increases, so does the modal dispersion and the reverse operation becomes more complex.

Controlling the incoming modes by wavefront shaping with an SLM, the transmission matrix can be obtained and it is possible to shape the output modes, as desired. This is operation aimed in this work.

2.2 Phase Optimization

Although interferometric [15, 69, 70] and phase conjugation techniques [35, 63] have been proved satisfactory to obtain TM, when considering multimode waveguides, their modal dispersion may set an obstacle to implement these methods as they can exhibit unpredictable mode coupling. Therefore, more exhaustive and thorough calibrations are necessary, besides the complex experimental setup.

Here, we propose a simple optical setup which relies in using a SLM to shape the input beam which will be guided, through a multimode fiber, to a photo detector where its magnitude information will be acquired.

In order to properly characterize the TM of the waveguides and shape the wavefronts according to specific targets, a semidefinite algorithm with a convex optimization solver is used. The greatest advantage of such programming method is the combination of the absence of a reference signal and the phase retrieval from intensity measurements, only. In short, it is possible to compute relevant portions of the TM around a focal

spot by feeding the SLM random inputs and acquire the intensity data, with a CCD. First proposed in 2015 [25], it has improved several fields of science, such as microscopy, crystallography imaging, among others [66].

Let us begin by considering a matrix A, which represents the input of the system and a complex matrix B, that combines information of magnitude and phase of the output. Both matrices are related through the TM of the medium considered.

As detailed in [25], the properties of A determine if the phase contained in B can be uniquely retrieved by the magnitude of the output vectors and if the stability holds for such solution.

Therefore, stating the problem only as it is, it falls under the conditions of a nonconvex problem. Although in the past [71], algorithms were proposed to converge to a solution, by introducing a convex relaxation, (PhaseCut [25]), the problem can be approximated by a semidefinite problem which can be solved with a quadratic optimization. Hence, the phase can be recovered with higher probabilities with independent A gaussian inputs. The PhaseCut relaxation simply conveys that the phase solution is a rank one Hermitian matrix and then the problem is reduced to a rank minimization over these semidefinite matrices.

Following the same notation as before [66], consider A and B as the respective input and output $M \times 1$ vectors, keep in mind that B contains phase and magnitude information of the output field and it is the product of the TM with the input, as described in the mathematical development below:

$$A = [a_1, \ldots, a_M]^T \tag{2.10}$$

$$B = [b_1, \ldots, b_M]^T \tag{2.11}$$

$$B = T \cdot A \tag{2.12}$$

A is, initially, treated in this method as random input phases that will be calibrated so the magnitude of B is maximized, which means controlling focus spots in the output field. The complex vector B is not fully known, only magnitude data can be acquired experimentally. As for the TM, it is our goal to determine it and then modulate the input fields to obtain a desired wavefront which will be guided by the multimode waveguide.

To make the notation more practical, let us take a single row of the TM as in equations 2.13 and 2.14, note that the z_m rows are the complex conjugate of T elements. The subscript m refers to the row of the matrix and the superscript m' is the column index.

$$T = \begin{bmatrix} z_1^\dagger \\ \vdots \\ z_M^\dagger \end{bmatrix} \tag{2.13}$$

$$z_m = \begin{bmatrix} (T_m^1)^* \\ \vdots \\ (T_m^{M'})^* \end{bmatrix} \tag{2.14}$$

Equation 2.12 was rewritten in function of z_m and $A^\dagger$, which is the Moore-Penrose pseudo inverse of A. Doing so, it is possible to observe, in equation 2.15, that there are two unknown variables, the phase information of b_m and the z_m elements. So it is useful to explicit both magnitude and phase of each row of B. Hence, vectors c_m contain its magnitude and vectors u_m, its phase $exp(-iarg(b_m))$. This composition can be seen in equation 2.16.

$$b_m = [A^\dagger \cdot z_m]^* \tag{2.15}$$

$$b_m = c_m \cdot [u_m]^* \tag{2.16}$$

Combining equations 2.15 and 2.16 follows that:

$$diag(c_m) \cdot u_m = A^\dagger \cdot z_m \tag{2.17}$$

By imposing the condition that u_m^i must be unitary and assuming N random input fields, it follows, in 2.18, an optimization problem but still with two unknown variables: the TM elements and the phase, z_m and u_m, respectively.

$$\begin{aligned} &\text{minimize } \|A^\dagger \cdot z_m - diag(c_m) \cdot u_m\|^2 \\ &\text{subject to } u_m \in \mathbb{C}^N, |u_m^i| = 1, z_m \in \mathbb{C}^M \end{aligned} \tag{2.18}$$

However, it is possible to manipulate earlier equations so the optimization problem is a function of the phase, only. Note in 2.17, z_m can be manipulated in function of u_m. This procedure is explicit in equation 2.19.

$$z_m = A \cdot diag(c_m) \cdot u_m \tag{2.19}$$

Replacing 2.19 in 2.18, the optimization problem reduces to one unknown variable: the phase. Once again, to make notation clearer, it follows that:

$$\begin{aligned}\|A^\dagger \cdot z_m - diag(c_m) \cdot u_m\| &= \|A^\dagger \cdot A \cdot diag(c_m) \cdot u_m - diag(c_m) \cdot u_m\|^2 \\ &= \|(A^\dagger \cdot A - \mathbb{I}) \cdot diag(c_m) \cdot u_m\|^2 \\ &= u_m^\dagger \cdot diag(c_m) \cdot (A^\dagger \cdot A - \mathbb{I}) \dot{(} A^\dagger \cdot A - \mathbb{I})^\dagger \cdot diag(c_m) \cdot u_m\end{aligned}$$

Using the following property for Hermitian matrices:

$$\begin{aligned}(A^\dagger \cdot A - \mathbb{I}) \cdot (A^\dagger \cdot A - \mathbb{I})^\dagger &= (\mathbb{I} - A^\dagger \cdot A) \\ P &= (\mathbb{I} - A^\dagger \cdot A)\end{aligned}$$

The previous calculation reduces to:

$$\begin{aligned}\|A^\dagger \cdot z_m - diag(c_m) \cdot u_m\| &= u_m^\dagger \cdot diag(c_m) \cdot P \cdot diag(c_m) \cdot u_m \\ &= u_m^\dagger \cdot Q_m \cdot u_m\end{aligned}$$

Where Q_m is an $N \times N$ matrix.
This previous manipulation allows us to rewrite 2.18 as in 2.20. Tr stands for the trace of the matrix.

$$\begin{gathered}\text{minimize } u_m^\dagger Q_m u_m = Tr(Q_m u u_m^\dagger) = Tr(Q_m U_m) \\ \text{subject to } |u_m^i| = 1 \text{ for i=1, } \ldots, \text{ N}\end{gathered} \tag{2.20}$$

The matrices defined as Q_m and U_m are semidefinite positive Hermitian and as $|u_m^i| = 1$, $diag(U_m)$ is also unitary. These facts support, the former mentioned, relaxation of the non-convex problem. If the optimization was to be proceed as in 2.20, the unitary rank of U_m would also be a constrain.

Given such relaxation, the problem is then, treated as convex and can be finally formulated as:

$$\begin{gathered}U_m = arg\ min\ Tr(Q_m U_m) \\ \text{subject to } U_m = U_m^\dagger,\ diag(U_m) = 1,\ U_m \succeq 0\end{gathered} \tag{2.21}$$

The optimization can be performed using conventional solvers, such as cvxpy. The retrieval of u_m is considered successful when high probability of recovery is met. In order to do so, the approach given by [25] is to account for N greater than $Mlog(M)$.

Once the problem is solved for u_m, it can be replaced in equations 2.17 and 2.15 and the TM of the medium can be found.

Thus, targets can be specified and the algorithm can properly feed the SLM properly modulated input wavefronts, according to the z_m elements retrieved.

Then, it is expected that the output magnitude corresponds to the targets, even when light is propagating in multimode waveguides.

The output intensities acquired after the optimization process are, then, compared to the ideal target. In order to perform a quantitative analysis of the focal spots generated, the optical constrast (OC) was evaluated. The OC was first defined in [72] and it is shown in equation 2.22, where $\bar{I}$ is the average intensity and σ_I is the intensity variance.

Another possible method to evaluate focus quality is simply to compare the intensity of the target position with the average intensity of the other positions of the reduced matrix.

$$OC = \frac{\sigma_I}{\bar{I}} \tag{2.22}$$

The OC is commonly used as a characterization parameters for speckle experiments which are the result of multiple interferences of partial waves. When their phases are uniformly distributed over 2π, the optical contrast is unitary. As a focal spot is actually a constructive interference obtained by the modulated fields, the greater the OC is, the better the quality of the generated focus is.

2.3 Theoretical Validation

In order to verify the model detailed in section 2.2, a theoretical validation was done. The goals with such simulation are to reproduce results found in literature [65], evaluate computation time and focus enhancement.

Random phase—only input matrices were given to the SLM and different focal spots were chosen. The output of each iteration is a vector which contains magnitude information for the determined focal surface. This vector will be later replaced for the experimental intensity measurements around that pixel area. The quadratic phase optimization was performed with the function “cvxpy.Minimize” according to equation 2.21.

Hence, the algorithm begins by setting an active area for the SLM screen which is the portion of the screen that is illuminated by the beam. The dark regions do not affect the wavefronts that is why they can be neglected. Then, such region was divided in smaller squares that define the number of degrees of freedom of the system. This means that the SLM screen is divided into square matrices -reduced matrices- that compose the surface to be optimized and each element represents one independent channel.

The same matrices dimensions follow for the CCD image, its screen is divided into smaller regions. So the number of elements of the reduced matrices also set the

resolution of the acquired images.

The collected acquired with create a database of phase and magnitude. An integer number n of trial fields, where $n = m(log(m))$ and $m = 8 \cdot 8$, should be modulated by the SLM to acquire enough data. Figure 2.2a illustrates these initial iterations.

Once the database is complete, the quadratic optimization is numerically computed with the function earlier mentioned, so that the TM can be retrieved and the optimized phase mask, generated. Then, the phase mask is loaded into the SLM so the input wavefronts are properly shaped to obtain the focal spot desired at the target, as depicted in Figure 2.2b.

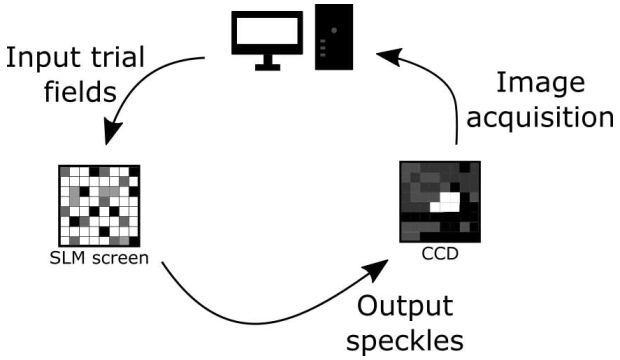

(a) Iterations of trial input fields.

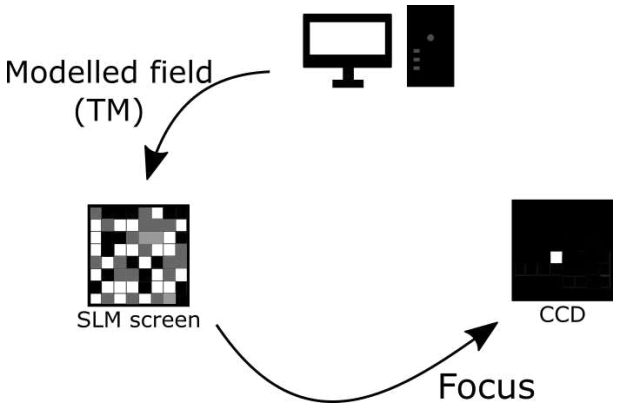

(b) Determining focus according to the TM.

Figure 2.2: Illustration of the algorithm iterations during theoretical validation. In (a), random input fields are tried and database is built. In (b), the optimized phase mask generates focus at the target.

The focus spots chosen in the simulation correspond to the positions (2,2), (3,3), (4,4) and (6,6) in the output reduced matrix whose elements are c_m, according to equation 2.16. In this case, number n of trials is 267.

The images, shown in Figure 2.3, are the results after optimization was performed, for the four focal spots earlier mentioned.

The average computational time to complete the simulations is 38 minutes. As for the focal spots, the optimization was able to properly enhance intensity in the correct area up to 80 % when comparing to an ideal focus. The optical contrast evaluated in the

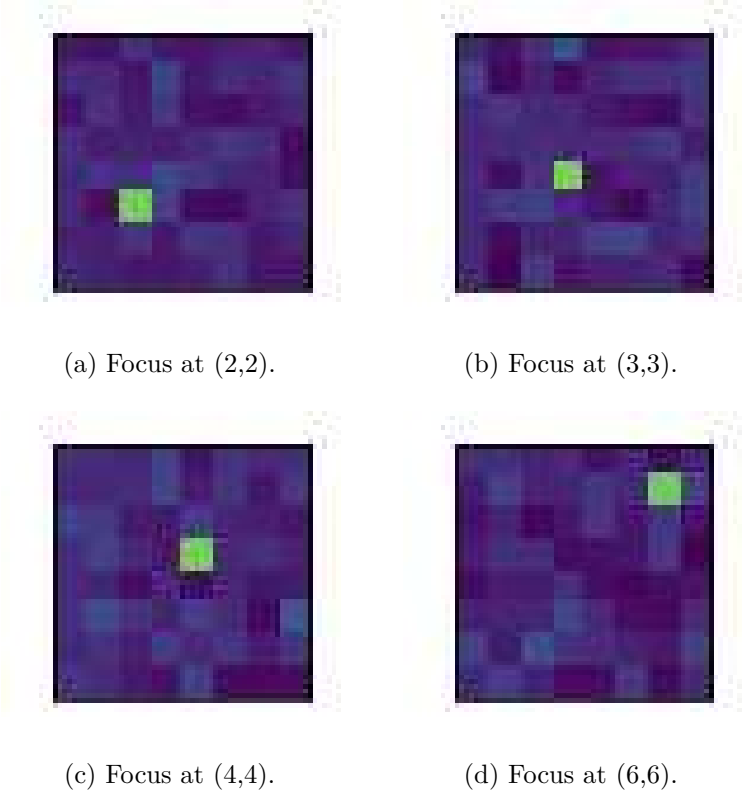

(a) Focus at (2,2). (b) Focus at (3,3).

(c) Focus at (4,4). (d) Focus at (6,6).

Figure 2.3: Results for the theoretical validation of the algorithm.

simulations for different targets can be found in Table 2.1. The values can be considered adequate since they are close to unity. The variation among the results are expected since the input fields are random matrices, therefore, as focusing depends on the phase and magnitude database built, each simulation has its own and that is why the focus obtained exhibits slightly different optical contrasts. Changes can also occur according to the modal distribution of the waveguide, in the experiment.

Table 2.1: Simulation of focusing experiments with a 8×8 reduced matrix, for different targets.

Target Position in the Matrix	Optical Contrast
(2,2)	0.95
(3,3)	0.89
(4,4)	0.98
(6,6)	0.91

Another parameter that requires examination is the number N of trials. Although it is well established in literature as aforementioned, a series of focus simulations were done to evaluated its influence on focus enhancement and optical contrast considering different matrices resolutions. The computational time was also included in these simulations. The results can be found in Figures 2.4b, 2.4a and 2.4c. These graphs exhibit

the correspond element size, in microns, to each matrix dimension. For a square matrix of order 4, each element from the matrix has a 12.5 µm, for a larger, 8×8 matrix, the dimension for each element is approximately 5 µm. Note that large matrix dimensions yield to smaller element sizes and greater achievable resolutions.

It is clear from the results shown that it is possible to improve focus quality by increasing either the matrices dimensions or the number of trials. However the computational has an exponential behavior to perform the optimization so, for a large number of trial field the time spent makes the experiment impractical. We can notice that for 8×8 matrices, the algorithm did not converge for 2n number of trials due to the heavy volume of data. That is why only information up to 7×7 matrices are shown for this number of inputs.

Aiming focus enhancements of about 80 % and optical contrast close to unit, matrices dimension lower than 6×6 are, then, disregarded. It is also noticeable that the rank of 7×7 did not converge as well as the even dimensions matrices.

Thus, the analysis of the graphs above proved that the more convenient number of trial fields is n being $mlog(m)$ and, in order to improve focus quality it is better to maintain such number of inputs and increase matrices dimensions, which will then lead to better significant better resolutions.

2.3.1 Multiple focal spots

The algorithm used to perform optimization returns the transmission matrix to generate a single focus, this can be a disadvantage when it is desired to image multiple spots or even a whole surface of a sample. Therefore, the algorithm was updated to map the whole effective area of the CCD in the shape of a reduced square matrix with given dimension.

Once the algorithm maps the speckle, the transmission matrix for every block of pixels in the reduced matrix is known. This means that it is possible to generate a focus in any desired position just by loading the optimal pattern on the SLM screen. This development of the method is valuable because it eliminates the calibration step, which can be time consuming, once the setup is not subject to strong perturbations.

Another great advantage of mapping the speckle is that multiple focal spots can be obtained simultaneously, without any further calibration.

Simulations were performed with a 8×8 reduced matrix, with a number N of trial fields in the calibration step to map the initial speckle. Where $N = mlog(m)$ and m is the dimension squared of the reduced matrix (m=8×8, in this case). After optimization, it was possible to obtain multiple focal spots, in any desired position, just my superposing their optimized phase transmission matrices.

Results can be seen in Figure 2.5. Note that the more focal spots are on, more

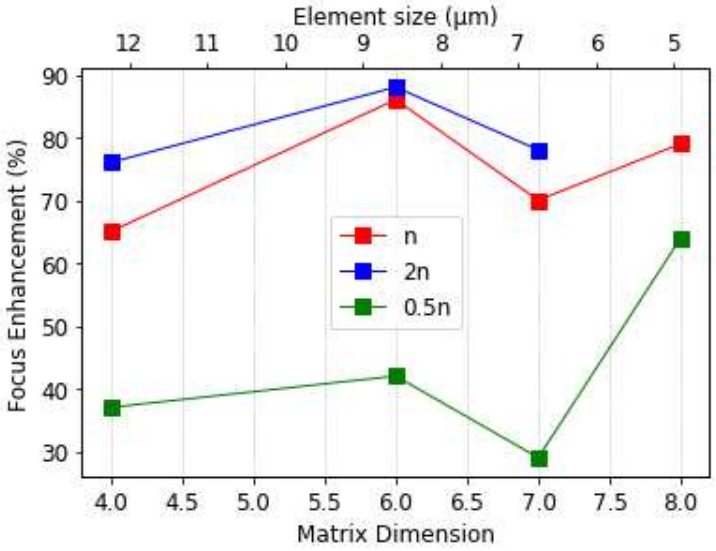

(a)

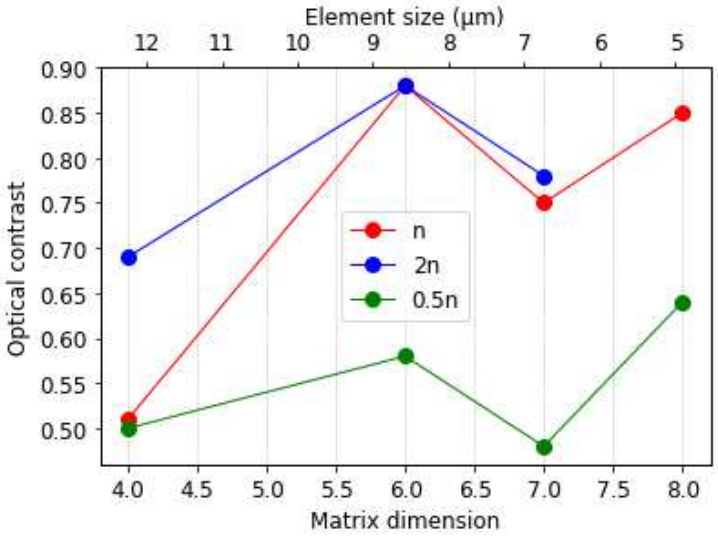

(b)

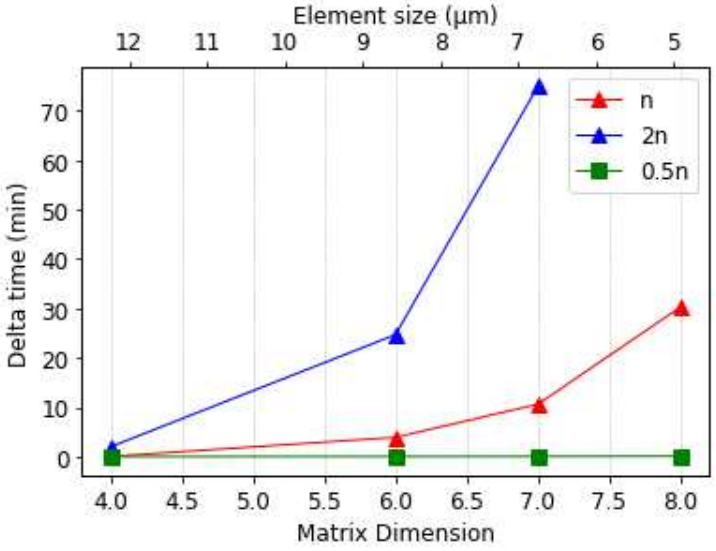

(c)

Figure 2.4: Quantitative analysis of focus enhancement, in 2.4a, optical contrast, in 2.4b, and computational time, in 2.4c. Three different integer number of trials (n), for a square matrix of $m \times m$.

background noise is expected. To minimize spurious intensity, it is plausible to increase the number of trial fields, so the optimization can be more efficient. Even though the calibration is computed only once, there is still a high computational time cost, so a balance between background noise and the amount of focal spots to be obtained simultaneously is in order.

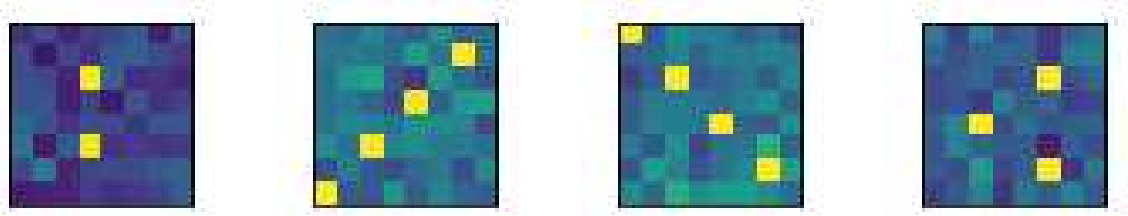

(a) (b) (c) (d)

Figure 2.5: Simulation results for multiple focal spots: In 2.5a, focus at (3,2) and (3,5). In 2.5b, focus at (0,0), (2,2), (4,4) and (6,6). In 2.5c, focus at (0,7), (2,5),(4,4) and (6,1). In 2.5d, focus at (2,3), (5,1) and (5,5).

2.4 Calibration for Experimental Setup

SLMs are powerful devices in this subject, therefore it is necessary to ensure its proper functioning. Hence, the calibration process for correctly shaping phase information in a phase—only SLM was carried out along with its experimental validation.

A Pluto Holoeye SLM device for visible range, from 420 nm to 700 nm, was used in this experiment. Its liquid crystal (LC) display has a resolution of 1920 × 1080 pixels and each pixel pitch is 8 μm. The active area was defined in 700 × 700 pixels considering the diameter of the coherent input beam

This device exhibits linearly aligned nematic crystals, which allow phase-only modulation without any influence on the amplitude of the incident beam. The LC molecules of the display are birefringent material and an applied voltage can control their refractive index and make them tilt to specified directions [73].

As the desired phase modulation depends only on the orientation of the LC cells, it is necessary to establish a relationship between the voltage applied and the pixels of the image sent to the SLM, which is actually a two-dimensional gray level mask. This procedure is executed with an lookup table (LUT) and this relationship is called the gamma curve. Interferometric and diffractive methods are commonly used to acquire it [74, 75]. The curve used in this experiment can be seen in Figure 2.6, and the maximum and minimum voltages applied are 3.40 V and 1.09 V.

To validate the gamma curve calibration, phase patterns were successfully tested in free-space, the results are shown in Figure 2.7. By using phase-only modulations,

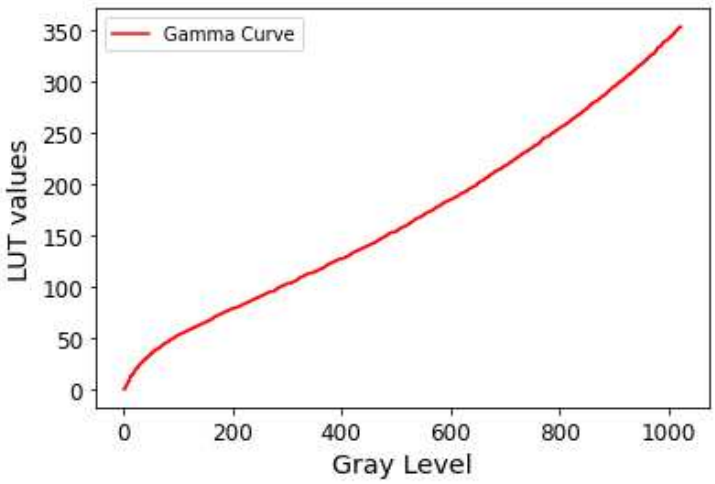

Figure 2.6: Gamma curve.

horizontal and vertical splits were fed to the SLM (Figures 2.7a and 2.7b) and phase difference between each side resulted in two distinct lobes. As for the ring and cross patterns, the projections are in Figures 2.7b and 2.7c and they are according to literature; the four spots in the cross pattern are expected when using a phase-only SLM, in visible range [23].

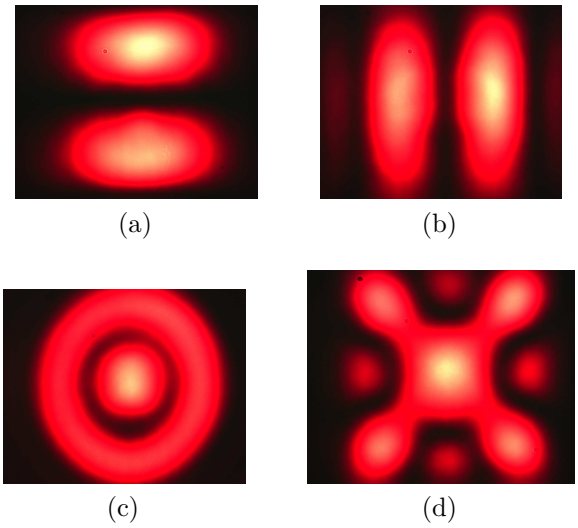

Figure 2.7: Gamma curve calibration in free space. Figure 2.7a shows the result of a phase mask with a horizontal split and Figures 2.7b and 2.7c, with a ring and cross pattern, respectively.

When aligning the first diffraction order in a single mode fiber (in infrared), the fundamental and high order modes (LP11 and LP21) could be excited using the phase modulation, as shown in Figure 2.8. It is also worth emphasizing that the first diffraction order has a reasonable 0.5 dB loss.

(a) (b) (c)

Figure 2.8: Mode excitation in a multimode fiber. LP01, in 2.8a, LP11, in 2.8b, and LP21, in 2.8c.

2.5 Conclusion

A concise review on multimode propagation of multimode fibers was presented at the beginning of this chapter so the modes of propagation could be better understood, in the context of this work.

Then, a method based on quadratic optimization was studied and validated. Focusing, in here, relied on a quadratic optimization method that generates a transmission matrix for the multimode waveguide, aiming a specific target for the focal spot. This procedure is executed by building a database of random input phase patterns and their respective magnitude information. Thus, the transmission matrix is able to characterize the modal dispersion of the waveguide in the setup and presents a relation between phase and magnitude data.

A spatial light modulator was used to shape the incoming wavefronts with the random phase patterns and, later, load the optimized phase matrix to also shape the beam so focus could be achieved at the output of the waveguide. The amount of controllable pixels on the SLM is what determined the degrees of freedom that the system will have. Also, each degree of freedom actually represents a modal base that will act on the modes of the multimode fiber, with intrinsic losses as a cost.

Fiber imperfections in both input and output can limit the resolution of imaging, once they will be considered in the acquisition of the intensity measurements with the CCD.

A theoretical simulation of the method which initially validated the algorithm developed. Then, in order to perform the experiments, a study on SLMss was done so it could be properly calibrated and coded. The first calibration measurements were in free space and the results of the modulated wavefronts ensured that the equipment was well functioning. High order modes of a single mode fiber in infrared were excited in the first diffraction order with a 0.5 dB loss. Therefore, an 8 pixels grating was set for the next experiments.

As the method was well validated and considered suitable for the objectives of

this project, it was used for the following experiments with different multimode fibers.

Chapter 3

Focusing Experiments

Once the method was theoretically validated, the experimental setup was assembled in the laboratory. For the focusing experiments, two different fibers that exhibit multiple modes in the visible range. The first fiber used was a MMF, with a 61.5 μm-core and the second one was a MCF with seven cores with 6.1 μm-diameter. The fibers were initially aligned so the output speckle is focused at the CCD.

The source used is a 633 nm Thorlabs laser, its power was properly adjusted so it overcomes the background noise and do not saturate the CCD. The beam finds the center of a Holoeye Pluto SLM, whose configuration is phase—only, and it is coupled onto the fiber Figure 3.1 shows the experimental setup earlier described.

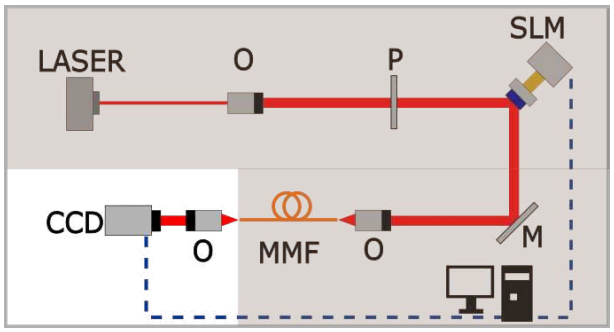

(a)

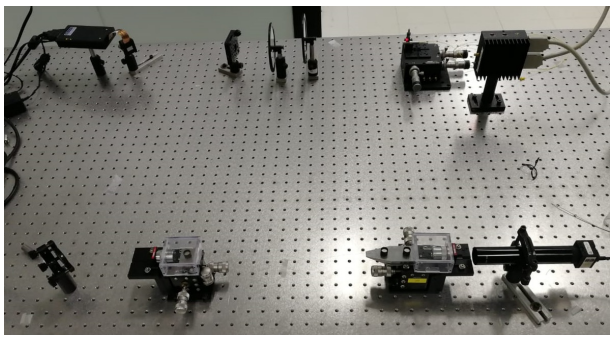

(b)

Figure 3.1: Scheme of the experimental setup in (a) and a laboratory picture in (b).

This first step consists on the trial inputs that will be used to optimize the proper pattern for focusing. Therefore, if the collected images randomly change due to such noises, it could greatly affect the quality of the focus pattern generated. But, if the noise is constant in time, the transmission matrix built takes it under consideration and such perturbation would not affect the final results.

Hence, a stability experiment was done, over the interested surface, to quantitative evaluate the progression of noise with time. A random phase mask was fed to the SLM, and the output intensity of the fiber was measured. It was found variations to up 20 % in magnitude, which can influence on the focusing results. Thus, a constant environment is necessary to perform the experiments. To be able to maintain such stable condition, an acrylic box was used to cover the whole setup. After placing it, the quadratic error of the measurement was taken in function of the time, as shown in 3.2. Note that the peaks in the graph might correspond to single stronger disturbances, especially in the beginning of the stability measurement when oscillations are greater but overall, by using the acrylic box, the system can be considered stable.

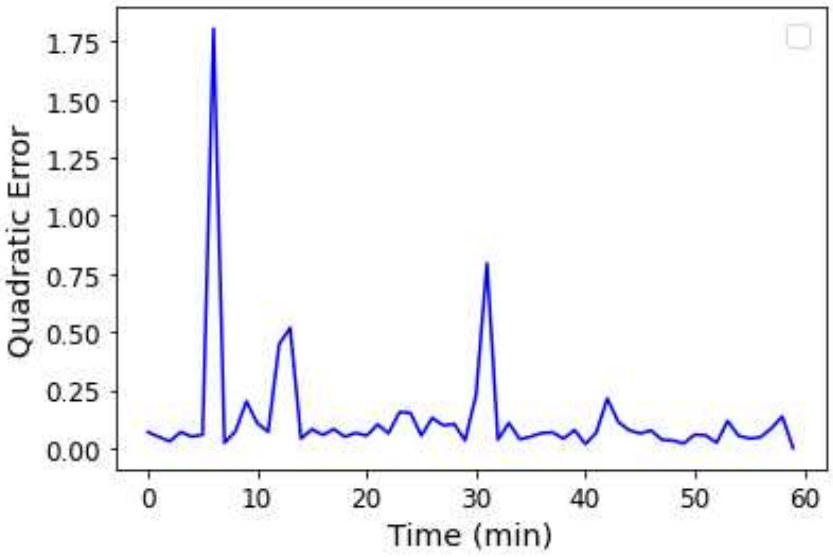

Figure 3.2: Stability measurements with a MMF at 633 nm.

The results for the focusing experiments using the MMF and the MCF are detailed in sections 3.1 and 3.2, respectively. An analysis of the resolution of the reduced matrix was carried out as well as quantitative measurements of the focus quality. In section 3.3, focusing was explored with a fiber bundle, assembled in the laboratory. This experiment is of great importance once it can bring direct applications in bio imaging.

3.1 Large core multimode fiber

Imaging experiments, for the 61.5 μm- MMF were performed with seven different matrix dimensions, with element sizes ranging from 22 μm to 50 μm at the CCD screen, which correspond to matrices with dimensions from 4×4 to 10×10.

Focus was generated for each position of the matrices, then, the procedure was repeated, at least five times and the average optical contrast for each experiment was evaluated as well as the standard deviation. The results can be seen in Figure 3.3.

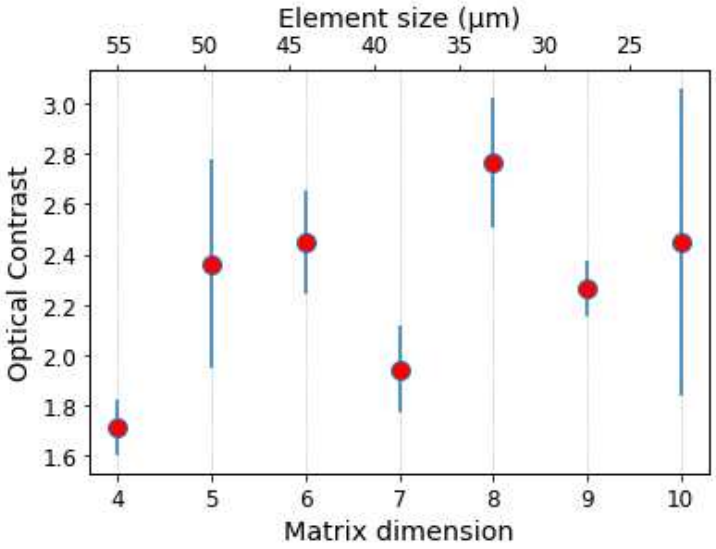

Figure 3.3: Optical contrast analysis for focusing experiments with a MMF, for varying matrices dimensions.

From the optical contrast results, we can infer that better focusing was achieved for the greater matrix resolutions. The matrices with dimensions 9×9 and 10×10 resulted focal spots with optical contrast not as high and with greater standard deviation. This impairment can be explained because the optimization time for the larger matrices is longer. As the time to perform the experiment increases, the system is subject to more instabilities which can affect the focus quality.

For low resolutions, such as the matrix 4×4, there is the lowest value for the optical contrast. This is an expected result, once larger focal diameters are more prone to divergence.

As for the 5×5 matrix, the high deviation suggests that instabilities occurred during the experiment and as divergence still has a significant influence, the system was not able to successfully overcome both disturbances and modal mixing of the fiber. So, a low optical contrast was obtained in this measurement.

Thus, a careful analysis must be made between optical contrast and resolution so imaging can be enhanced. Another relevant factor to taken into account is the time for optimization. Although we can achieve finer resolution as we increase the reduced matrix

dimensions, it is necessary to consider the computational time taken. From the simulations (Figure 2.4c) and from the theoretical analysis, a exponential relation is expected between the time for optimization and the matrix dimensions. So, for the same resolutions studied, the optimization time was measured. The results can be seen in Figure 3.4. The expected exponential behavior was experimentally found.

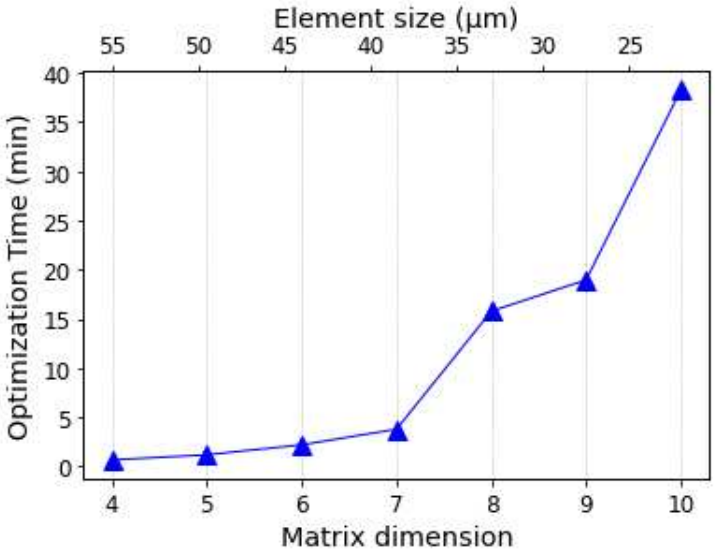

Figure 3.4: Time to optimize phase matrices in focusing experiments with a MMF, for varying matrices dimensions.

To better study how well the focus spots can be generated in different spatial positions, a 10×10 reduced matrix dimension was chosen so that each element corresponds to a quarter of the initial speckle, which means that each small square from the output image corresponds to, approximately, $22\,\mu$m. Figure 3.5 shows the result of the experiment. In 3.5a, the output speckle of the fiber is exhibited. As modal interference can rapidly change the output speckle throughout the measurements, the optical fiber was kept strained and inside a box to minimize mechanical perturbations and decrease errors in the optimization process.

The speckle was divided in four quadrants, aiming to obtain single focus in each one of them. Figures 3.5b to 3.5e show the focuses obtained. Focus at the first quadrant is visually the less accurate, however, it is expected that it would be slightly deviated once the initial speckle does not have a perfect circular shape: there is a deformation right at this quadrant. The average optical contrast is 1.8.

As the previous results proved to be possible to set the position of the focal spot, finer experiments were proposed. For those two matrices resolutions were chosen to analyze focusing in different targets: 8×8 and 10×10, which corresponds to focal diameters of 27.4 µm and 22 µm, respectively. The first one was chosen because it presented the highest value of optical contrast while the second was chosen because it is the better resolution obtained, even though there is a computational time cost.

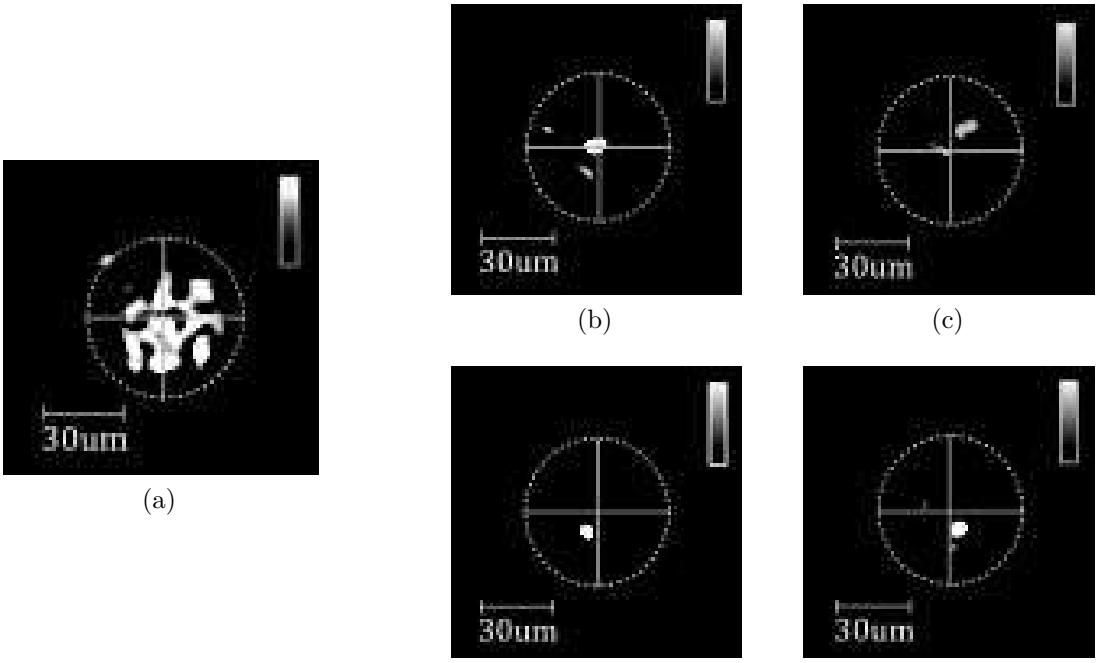

(a) (b) (c) (d) (e)

Figure 3.5: Initial output speckle in (a). Focus after optimization in the 1^{st}, 2^{nd}, 3^{rd} and 4^{th} quadrants, respectively, shown in Figures (b), (c), (d) and (e).

The results from focusing with a 8×8 reduced matrix can be seen in Figure 3.6. The optical contrast found for all focal spots were summarized in Table 3.1 and agree with the experimental data from the previous experiment.

As mentioned before, it not possible to control the dark regions of the SLM and the same reasoning applies here. The targets can only be chosen in positions that are illuminated. Four different targets were set in this experiment. For each one, it is necessary to compute a TM so the convergence can be obtained in different positions.

Table 3.1: Focusing experiments with a MMF, with a 8×8 reduced matrix, for different targets.

Target Position in the Matrix	Optical Contrast
(5,4)	2.3
(4,4)	2.3
(3,4)	2.1
(4,5)	2.0

The four targets were met in the experiment which shows that the applied method can be used to spatially tune the convergence spot. It is worth noting that the initially speckle can vary once modal mixing depends on mechanical disturbances, temperature variations and bending of the fiber. Even though, the TM for each situation still presented satisfactory results.

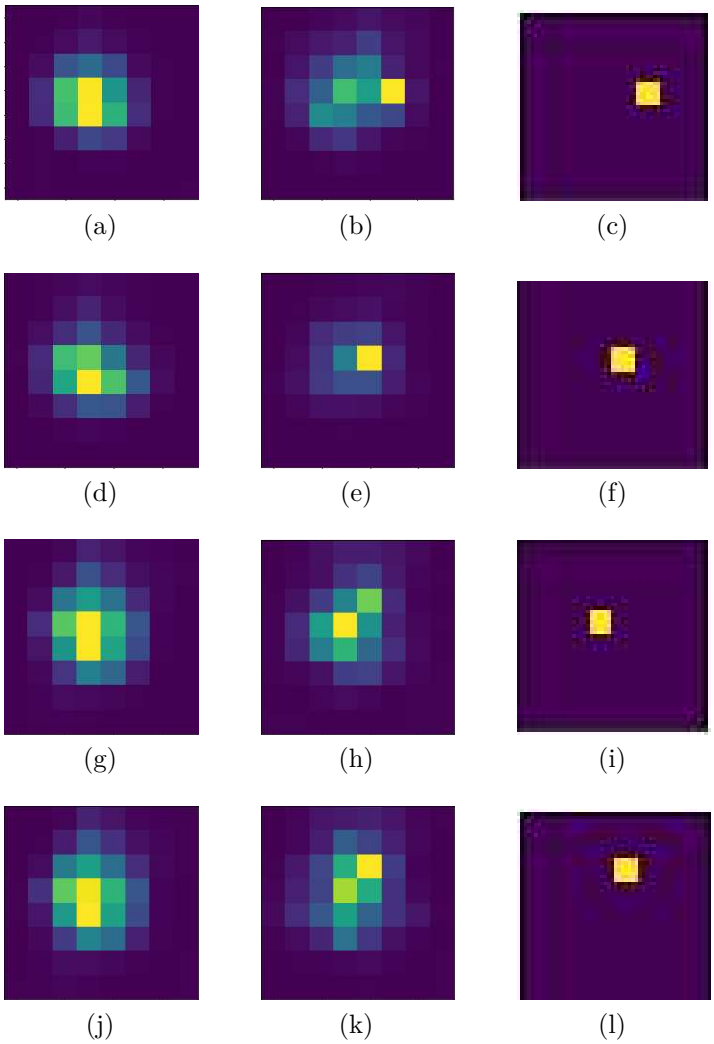

Figure 3.6: Focal spots generated for different target with a 8×8 reduced matrix. In 3.6a, 3.6d, 3.6g, and 3.6j, the initial pattern. In 3.6b, 3.6e, 3.6h and 3.6k, the focusing results for positions (5,4), (4,4), (3,4) and (4,5), respectively. In 3.6c, 3.6f, 3.6i and 3.6l, the focus targets.

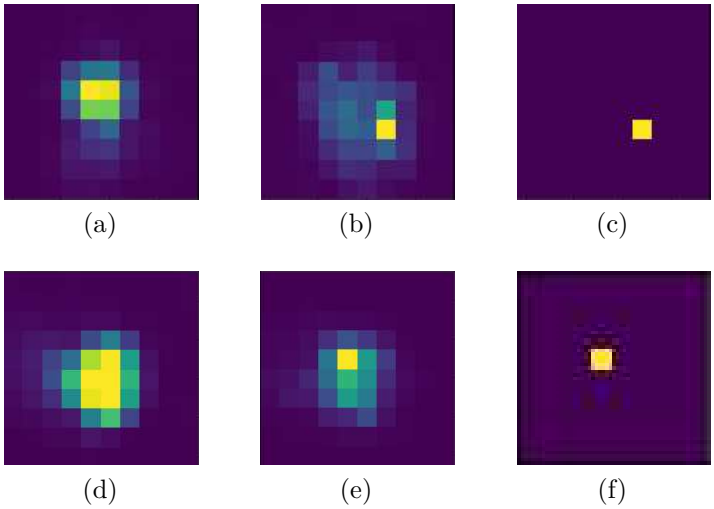

Figure 3.7: Focal spots generated with different initial output intensity distribution. A 10×10 reduced matrix was set. In 3.7a and 3.7d, the initial pattern. In 3.7b and 3.7d, the focusing results. In 3.7c and 3.7f, the focus targets.

Aiming even finer resolutions, the 10 matrix was experimented. Two targets at (7,4) and (5,6) were set for this case, once longer computational time is required.

In Figure 3.7, the reduced matrices of this experiment are shown. It is possible to observe the initial speckles in Figures 3.7a and 3.7d and the convergence spots at the predetermined spacial location of the matrix in Figures 3.7b and 3.7e. In order to better comprehend the results, the ideal targets are presented in Figures 3.7c and 3.7f.

Focal spots were again successfully generated, independently of the initial output intensity distribution.The optical contrast found are according to the ones earlier presented, around 2.4, for this resolution.

3.2 Multicore Fiber

Once the MMF was explored and focusing was achieved with this fiber, a multicore fiber was inserted into the experimental setup. Each of the seven cores has a 6.1 μm diameter and it presents a multimode profile in the visible range. The same procedures earlier discussed were applied for this fiber. However, we aimed to generate focus so only predetermined cores are illuminated.

In Figure 3.8a, it is possible to observe the initial output of the fiber, in which all seven cores are illuminated. For the analysis, the cores were numbered from one to seven, as depicted in Figure 3.8b.

Three different phase masks were optimized to excite three of the seven cores. Note that is necessary a resolution of the same figure as the diameter of the core, which corresponds to a reduced matrix of 10×10.

It was possible to generate focus at the preset cores and the outputs intensity

distribution can be seen in 3.8c, 3.8d and 3.8e. ,The optical contrast for each one indicates satisfactory quality and agrees with the results from the MMF. The exact results can be found in Table 3.2.

Table 3.2: Focusing experiments with a MCF to illuminate cores individually

Core Number	Optical Contrast
7	2.7
6	3.0
2	3.0

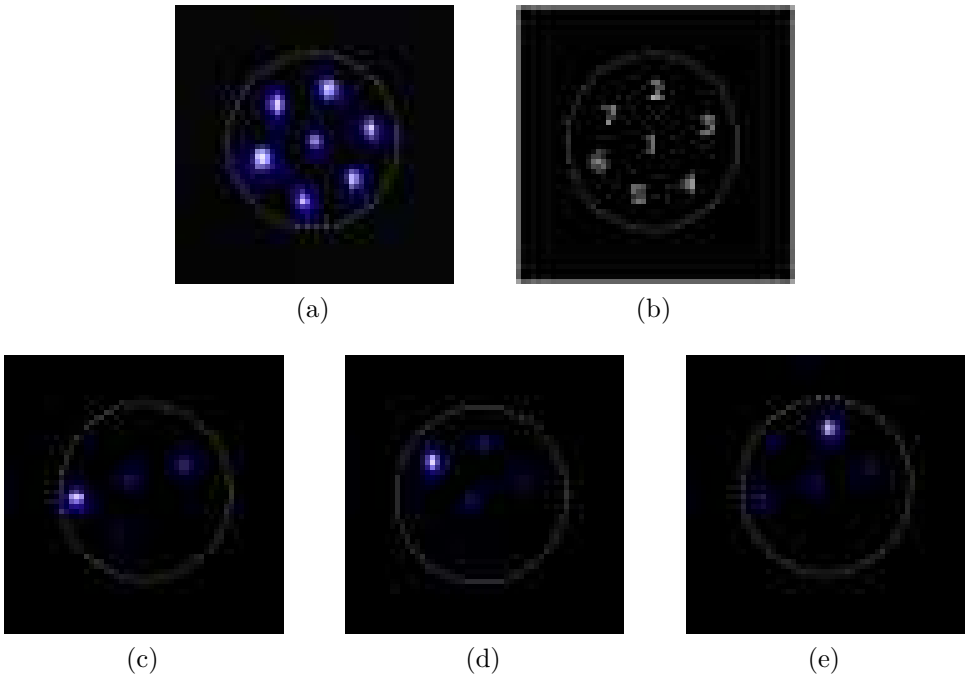

Figure 3.8: Initial output in (a) and single cores were numbered in (b). Focus after optimization in cores numbered 7, 6 and 2, respectively, shown in Figures (c), (d) and (e).

Then, a superposition of pairs of phase masks was loaded into the SLM and, as expected, it is possible to observe the corresponding cores being illuminated. However, when the superposition is performed, the noise also increases, thus, it was not possible to excite the three cores simultaneously. Figure 3.9 shows cores 6, 7 and 2 being illuminated, two at once.

Still, the possibility of independently tuning the cores of the fiber in the visible range is promising in applications such as photonic integrated circuits, bio sensing and even as neural probes [76].

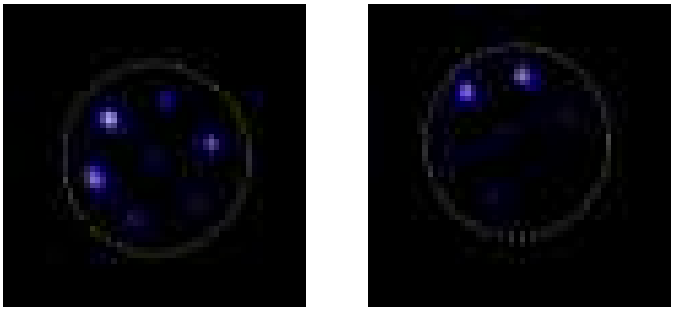

(a) (b)

Figure 3.9: Simultaneous focus at: cores 6 and 7, in (a); cores 7 and 2 in (b).

3.3 Multimode Fiber Bundle

One of the applications for the imaging experiments is the fiber endoscope. Fiber endoscopes have been useful tool in biological fields for the diagnose of samples. One of the challenges encountered in to enhance and tune the convergence spot at the distal end of the endoscopes, so finer analysis can be carried out, with smaller or even *in-vivo* samples.

The experimental setup that we propose in this work can explore this application, once, it can tune the spacial position of the focal spot. Also, as it is a stable system, there is no need to monitor the end of the waveguide after its transmission matrix has been retrieved.

To explore these features, an endoscope, in Fig.3.10, was fabricated from a from a bundle of 130 MMFs. A rigid tube was used to gather the fiber that were 15 cm-long. The rigid tube improved the stability of the setup and a robust tool it is also desirable for biological imaging.

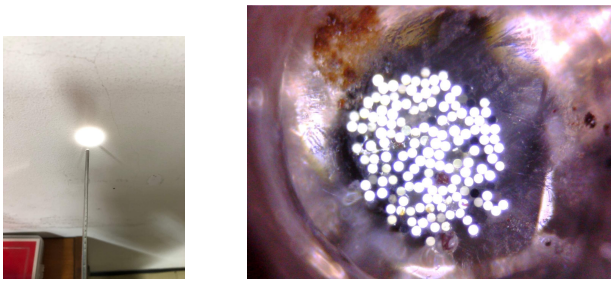

(a) (b)

Figure 3.10: Prototype of a fiber bundle endoscope illuminated with a white source: 3.10a. Cross section of the multimode fiber bundle endoscope: 3.10b.

An initial experiment was tested, using the prototype presented. The same experimental setup was used, but this time, with the fiber bundle as the waveguide (Figure 3.11). The active area of the CCD was set to 600×600 pixels, which means that

the dimensions for each element of the TM is going to be different than the values found for the fibers studied in the previous sections of this work.

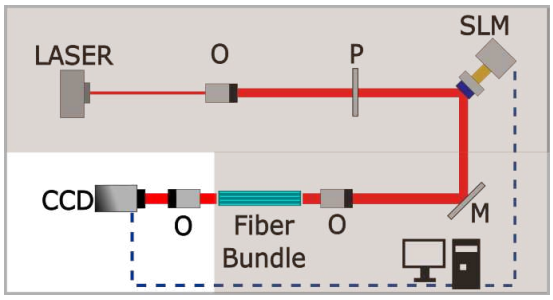

Figure 3.11: Experimental setup with the fiber bundle.

For this first focusing optimization, a reduced matrix of 6×6 with each square-element has a 220 µm side. The target for focusing was set at the position (3,3) of the reduced matrix, once it was a well lit spot. Focus optimization was successfully achieved by acquiring the corresponding transmission matrix of the fiber endoscope, as it is observed in Fig. 3.12. The optical contrast obtained was up to 1.38.

However, the optimization time was up to 30 minutes. It shows a significant computational cost when comparing to both MMF and MCF, when the same reduced matrix required less than 5 minutes to optimization. The escalating optimization time was expected due to the substantial increase in the number of modes in the bundle. As mode mixing is stronger, the TM responsible for tuning convergence spot is more difficult to be optimized.

Nonetheless, a fast imaging is desirable if biosensing applications are aimed. Thus, an analysis of reducing in half the number of random input fields to make the database for optimization was made in the following experiments.

Once there were positive results for the prototype. New bundles were fabricated using a stainless tube with 3.17 mm outer diameter and 1.76 mm inner diameter. Fiber cores with 60 μm-diameters were used and the amount of fiber cores inside the bundles was also varied so the influence of the amount of fibers, and therefore the number of modes, could be discussed, as well. Bundle containing, approximately, 70 and 200 fiber core were assembled. They will be referred in this section as partially filled, for the 70 fiber cores bundle, and filled, for the 200 fiber cores bundle. The ends of the tubes with the fiber were glued with an epoxy UV to assure stability.

After assembling the instruments, the cross section of the bundles was polished in order to obtain clear intensity profiles at their output. The pictures in Figure 3.13 show the polished cross sections for both fiber bundles.

The focusing experiment began with the partially filled bundle with 60 μm-fibers(3.13a) using a 6×6 reduced matrix, which corresponds to a 220 µm resolution. The resulting images for this case can be seen in Figure 3.14. The target was set to the (3,5)

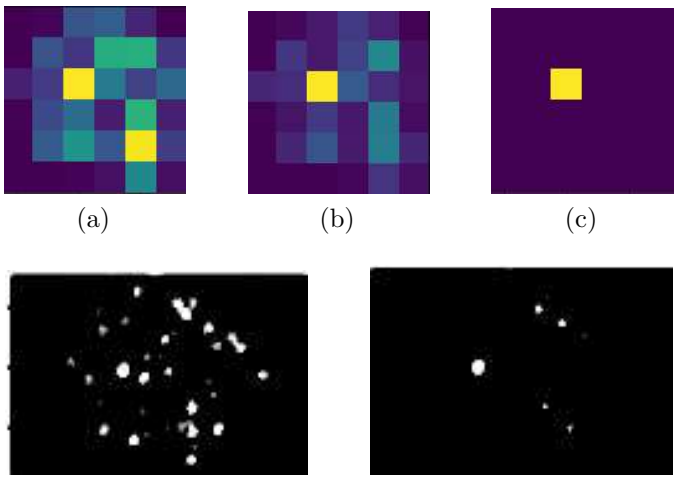

(a) (b) (c)

(d) (e)

Figure 3.12: The initial pattern of the fiber endoscope in 3.12a. The resulting pattern after optimization in 3.12b and the desired target, in 3.12c. The CCD images of the initial speckle and the optimized focus are shown in 3.12d and 3.12e.

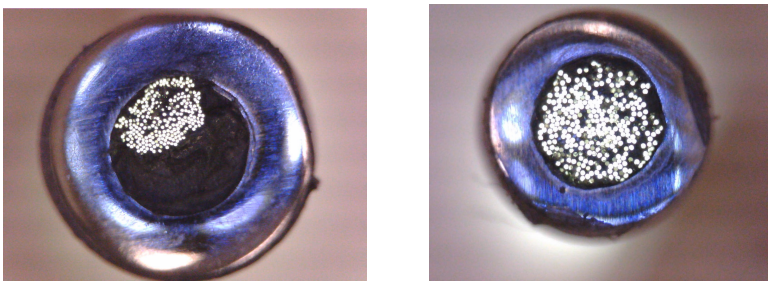

(a) (b)

Figure 3.13: 60 μm fiber bundles: In 3.13a, approximately, 70 fibers inside the bundle and in 3.13b, approximately, 200 fibers.

position to take advantage of the well illuminated region. We emphasize that the database used for optimization was decrease to half so computational time could be decreased.

The initial speckle, in Figure 3.14a, clearly shows the disordered cores in the bundle. It is also possible to observe that, although the fibers were glued for mechanical stability, the longitudinal distance of the cores is different. In other words, each core presents a different divergence pattern which makes focusing harder.

Still, after optimization, we can notice in Figure 3.14b a tendency for focusing in the preset region (target in 3.14c). The resolution, here studied, is larger than a single core, so imaging was satisfactory.

The optical contrast evaluated was 1.50 and the computational time decreased to, approximately, 1 minute. So, even though the database was reduced, it was still possible to perform the imaging experiment with an adequate focus quality (greater than 1). Then, it was settled that, as the optical contrast did not suffer any crucial impairments, the database will be reduced to half so imaging with the fiber bundle is more efficient.

An image from the CCD screen, both before and after focusing, is presented in Figure 3.14d, on the left and right, respectively.

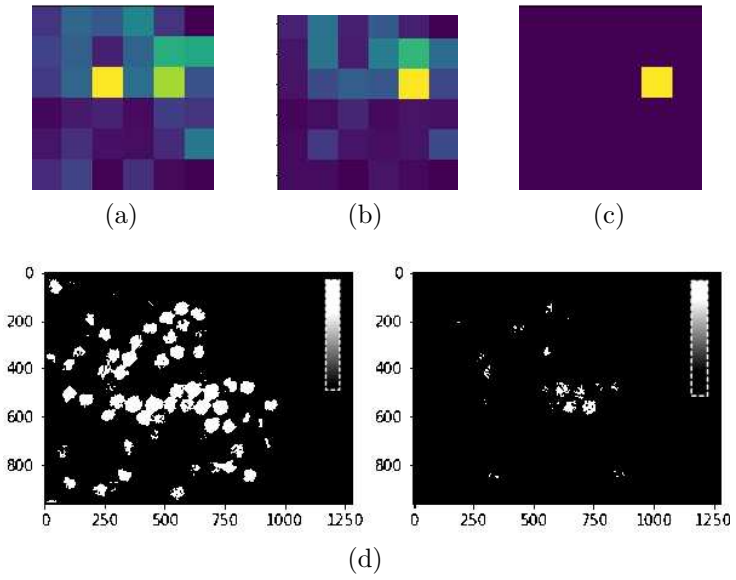

Figure 3.14: Focusing with a 60 µm partially filled fiber bundle with a 6×6 reduced matrix. The initial speckle and obtained focus in 3.14a and 3.14b. While the set target is in 3.14c and the image from the CCD in 3.14d.

Then, experiments were performed varying the resolution. Reduced matrices of 8×8 and 10×10 which corresponds to elements with 165 µm and 132 µm, respectively were set and focal spots were targeted at different positions.

Figure 3.15 shows the results for focusing with 165 µm resolution. The target, in this case the position (4,4) in the reduced matrix. The computational time for this optimization was 2.5 min and the optical contrast obtained was 1.3.

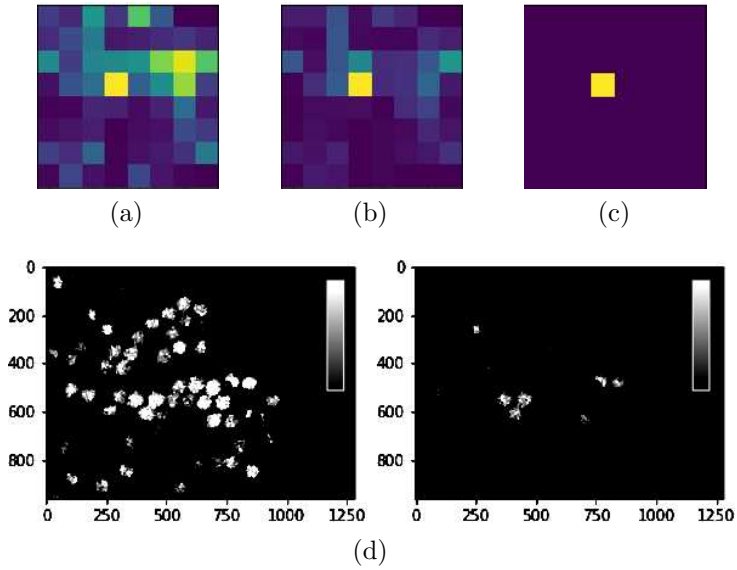

Figure 3.15: Focusing with a 60 µm partially filled fiber bundle with a 8×8 reduced matrix. The initial speckle and obtained focus in 3.15a and 3.15b. The set target is in 3.15c and the image from the CCD in 3.15d. On the left, the initial speckle and on the right, the focused image.

In Figure 3.16, the results for focusing with a 132 µm resolution can be found. The target (3.16c) was set to (3,4) in this experiment. The initial speckle is shown in Figure 3.16a and the focus obtained in Figure 3.16b. Although the focus was not positioned exactly as set by the target, we still considered the experiment successful when the resolution is taken into consideration. The optical contrast agrees with this reasoning as it was evaluated in 1.62.

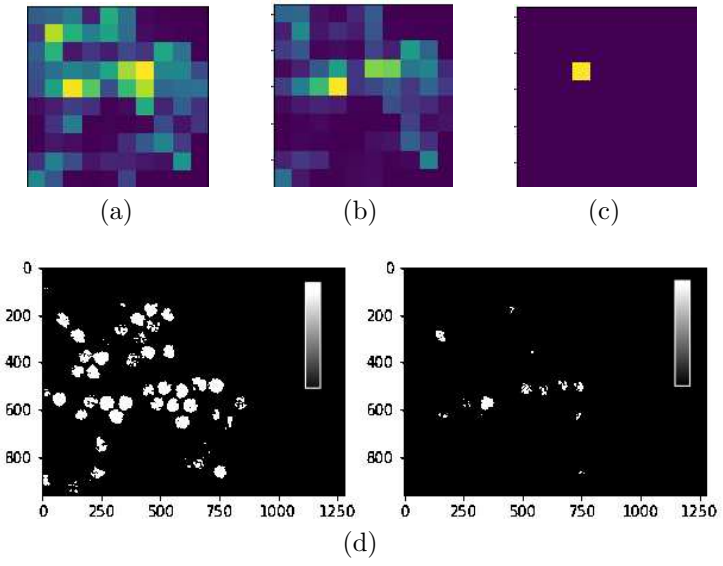

Figure 3.16: Focusing with a 60 µm partially filled fiber bundle with a 10×10 reduced matrix. The initial speckle and obtained focus in 3.16a and 3.16b. The set target in 3.16c and the initial (left) and focused (right) images from the CCD, in 3.16d.

To summarize the data collected for focusing experiments with the partially filled fiber bundle, Table 3.3 is presented. We can see that the objective to make imaging faster without impairing focus quality was met.

Table 3.3: Focusing experiments with a partially filled fiber bundle

Matrix Dimension	Optical Contrast	Optimization time (min)
6×6	1.50	1
8×8	1.30	2.5
10×10	1.62	5.8

Finally, the fiber bundle approximately filled with fiber cores of 60 µm (Figure 3.13b) was inserted into the setup.

Even with a more numerous fiber core bundle, the computational time for the imaging experiments remained within the same order of the results with the partially filled bundle as we continued on using half the database in order to speed up optimization. At this time, only the 10×10 (132 µm-resolution) was used once it was known from the previous experiment that it presented the greater optical contrast.

Different targets at positions (4,1), (4,4) and (7,2) of the matrix were set and the convergence obtained in each experiment were compared, as well as the optical contrast for each. So the images are more clearly presented, only the initial speckle and focus acquired are shown in the results in Figure 3.17.

Although subtle, it is possible to observe convergence at the set targets when the results are compared with the initial speckle. It mean that the phase masks were correctly optimized and the convergence was spatially tuned, as experimented in the MMF and MCF experiments. Table 3.4 shows the optical contrast for each position.

Table 3.4: Focusing experiments with a filled fiber bundle, using a 10×10 reduced matrix.

Target Position	Optical Contrast
(4,1)	1.49
(4,4)	1.33
(7,2)	1.44

To justify choosing targets in the bright areas of the spots, an experiment where the position (7,6) was set as target was performed. The resulting images in Figure 3.18 show that optimization was quite poor and optical contrast for this situation was 0.56. Such dark regions can come from fabrication issues as fibers can break when joined into the rigid tube.

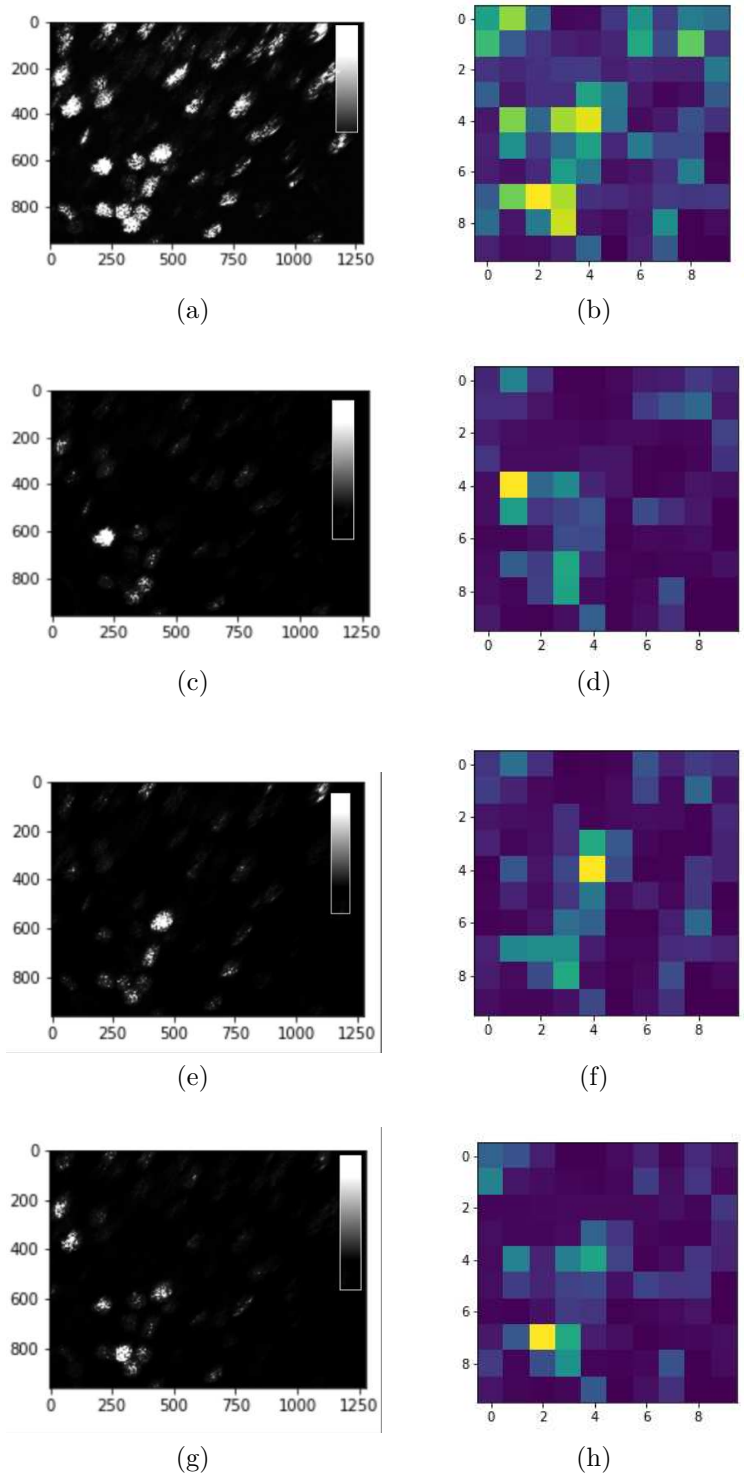

Figure 3.17: Imaging with the filled fiber bundle at three different targets. In (a) the CCD image for the initial speckle and in (b) its corresponding reduced matrix. The CCD images after optimization are shown in the following (c), (e), and (g), for the targets at (4,1), (4,4) and (7,2), respectively. The corresponding reduced matrices are shown in (d), (f), and (h).

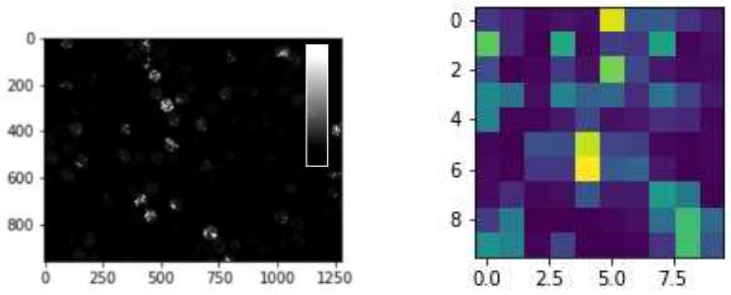

(a) (b)

Figure 3.18: Attempt to obtain focus at a dark region, at position (7,6). In (a) and (b), the CCD and reduced matrix images, respectively. Optical contrast was below 0.6.

3.3.1 Multiple focal spots with the fiber bundle

The final experiments with the fiber bundle was to demonstrate simultaneous convergence spots. The same fiber bundle containing approximately 200 fiber cores was used in this part of the experiment. The phase masks from focusing at positions (4,1), (4,4) and (7,2) were combined in order to excite two focal spots simultaneously. A superposition of each TM was made and this new phase pattern was loaded into the SLM with no additional calibrations.

It was already known from the results for the multiple core excitation, with the MCFs, that the noise for each single focus would be combined and become more relevant, that is the reason that only pairs of focal spots were chosen for this experiment.

Even with all the expected cumulative noise, focal spots could be successfully obtained with such TM combinations. Figure 3.19 shows the results of the experiment. The initial speckle (in Figure 3.17b) had no changed. The first pair tested was (4,1) and (7,2). The final distribution, in the CCD screen and in the reduced matrix presentation, can been, respectively, in Figures 3.19a and 3.19b. The (4,1) position appears more bright than the (7,2), however, when obtaining the single focus, this spot already had a higher average intensity, so it repeats in the combination.

As for the pair (4,1) and (4,4), the convergence spot is vivid on the CCD screen, seen Figure 3.19d. The respective reduced matrix is shown in Figure 3.19c. Finally, the pair (4,4) and (7,2) is presented in Figures 3.19f and 3.19e again with well marked convergence spots.

The optical contrast evaluated for each one of the pairs can be found in Table 3.5 and can quantify the experiment. All results are indubitably greater than 1, which supports the experiments.

The results here shown points that the fiber bundle proposed is a promising instrument in imaging applications. Even with disturbances, the ability to tune single and multiple convergence spots are clear advantages of the proposal, besides the well evaluated optical contrasts and suitable optical intensity.

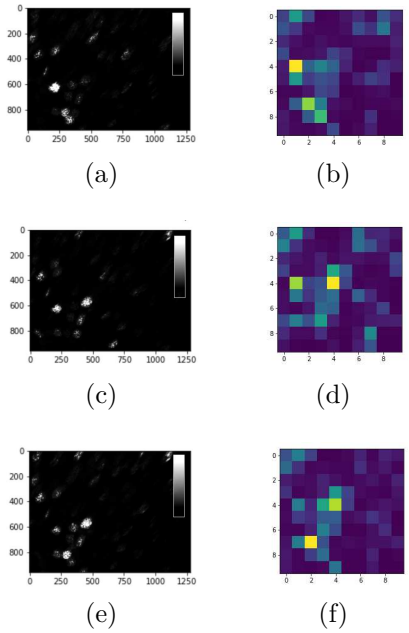

Figure 3.19: Simultaneous focus imaging. Focus at (4,1) and (7,2) in the CCD image and in the reduced matrix shape at 3.19b and 3.19a, respectively. Focus at (4,1) and (4,4) in the CCD image and in the reduced matrix shape at 3.19d and 3.19c, respectively. Focus at (4,4) and (7,2) in the CCD image and reduced matrix shape at 3.19fand 3.19e, respectively.

Table 3.5: Optical Contrast for simultaneous focal spots, using a 10×10 matrix.

Focus Position	Optical Contrast
(4,1) and (7,2)	1.43
(4,1) and (4,4)	1.31
(7,2) and (4,4)	1.43

3.4 Conclusion

In the first focusing performed, a multimode fiber with 61.5 μm core was used. Choosing this fiber as the waveguide enabled multiple modes to be excited in 633 nm and the initial results are according to the theoretical validation.

Seven different resolution were studied, from 22 µm to 50 µm and focus for each of them was obtained. They were evaluated according to their optical contrast, which considers the variance in the intensity distribution of the image. All results are above 1.0. This is an indicative that clear focus spots were acquired and they follow a normal distribution. The results from the MMF are an important part of this work, once they show that strong modal mixing can be properly characterized and focus with dimensions in the order of tens micro meters can be achieved.

Along with the resolution, the computational time for optimization was also considered in the analysis. Then, focusing was performed by spatially exploring the focal targets with a multicore fiber. This fiber has seven cores with a 6.1 µm-diameter each.

Resolution was set so each element of the reduced matrix is about 20 µm. It was shown that, by focusing, it was possible to illuminate cores individually, however, with a finer resolution better results focal spots could be produced. The need of a thinner resolution comes from the small diameter of each core.

Also, motivated by the theoretical analysis that phase masks could be combined to generate simultaneous focal spots, pairs of cores were excited by combing the transmission matrix earlier acquired for each one. It is interesting to analyze that the average optical power does not decrease substantially, but only the intensity distribution changes.

The study of fiber bundles showed that the method is also efficient to induce focus with disordered gathering of fibers. Fiber bundles with different quantities of fiber cores (approximately, 70 fiber cores and 200 fiber cores) were assembled in the laboratory and focus was acquired for both of them in different spatial positions. Each element for the reduced matrix of the CCD now corresponded to, approximately, 130 µm.

As the fiber bundle is a highly multimode media, optimization became more complex and, it was necessary to make a balance between the amount of data for optimization and focus quality. So, it was judged that the best strategy would be to reduce the database in half to proceed with imaging. Still, focus was clearly generated.

A superposition from the phase masks was also performed and pairs of convergence spots were also generated with the fiber bundle.

Chapter 4

Coupling Experiments with a Graded Index Fiber

After studying focusing with MMFs and MCFs, interest in GRIN fibers arose due to their refractive index profile and a lesser number of modes. Although, GRIN fibers have been applied in communication systems, non linear phenomena such as self-imaging have been studied with this type of waveguide. Such features make them convenient waveguides to be used in the imaging experiments.

Self-imaging occurs in GRIN fibers because its propagation function can be reduced to delta functions of the propagating distance, it leads, then, to constructive interference which can be comprehended as periodic well defined focal spots. Besides, this phenomenon covers any partially coherent input field [49, 77].

Therefore, GRIN fibers are fair subjects of interest when it comes to lensed fibers, focusing fibers tips, among others [54]. Especially, lensed fibers enables tuning the divergence beam angle, the dimensions of the focal spot, besides the focal length [55, 56]. The fabrication of lenses on the tip of the fibers has been theoretically studied in recent studies found in literature [58].

However, most studies are limited in the near infrared or infrared frequencies of the electromagnet spectrum due to mode selection and size of the devices. Besides, it is well known that the visible region of the spectrum brings mode mixing.

4.1 Focusing with a GRIN fiber

In this part of the work, we apply the same method of phase-shaping the wavefronts, in the visible range, to obtain focus with a GRIN fiber without the need to fabricate any lenses at their distal end. We aim to overcome modal mixing by obtaining a proper phase mask through optimizing the TM of these fibers.

The experimental setup assembled in this part of the work is equivalent to the

one presented before and it was just updated with a 62.5 µm-core multimode GRIN fiber, as depicted in Figure 4.1. It is still the simple free space configuration where reference beam is needed. The polarized input beam, at 633 nm, is collimated and expanded to fit the active area of the screen of the SLM. When the beam is reflected on the SLM screen, it is coupled into the fiber, by objective lenses.

Eventual mechanical disturbances were still minimized by covering the experimental setup with the acrylic box.

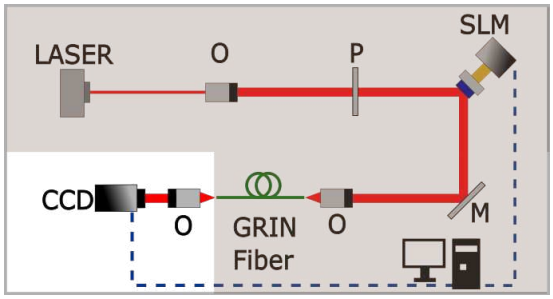

Figure 4.1: Experimental setup for focusing with the GRIN fiber.

The optimization of three different phase masks was performed. The focal spot targeted for these masks was set at the center of the initial speckle due to light convergence and optimized power, consequence of the gaussian profile exhibited.

Then, three different phase masks were generated for this experiment, aiming different diameters for focal spot: 29 µm, 24 µm and 20 µm. To be able to achieve such dimensions, the active area of the CCD was 130×130 pixels, while the dimensions of the generated TMs were 9×9, 11×11 and 13×13.

Focusing was accomplished for each of the pre-established target diameters. Table 4.1 shows the optical contrasts for each focal spot. All evaluations are greater than 1.0, thus it can be concluded that focusing was efficiently performed. Besides those results, Table 4.1 also displays the output power before and after focusing. The power measurements mean that the images do not show any filtering effects, but only a change in the intensity distribution, which is the focusing.

Table 4.1: Focusing experiments with a GRIN fiber with varying resolution.

Phase matrix dimensions	Focus diameter (µm)	Optical contrast	Total output power (dB) Before	After
13×13	20	1.1	-23.43 ± 0.17	-23.38 ± 0.42
11×11	24	1.2	-22.79 ± 0.14	-22.72 ± 0.08
9×9	29	1.1	-22.25 ± 0.22	-22.16 ± 0.21

The initial output speckle of the multimode GRIN fiber can be seen in Figure 4.2a. The focusing results for each resolution presented in the table above are seen in Figures 4.2b to 4.2d, with their respective scale bars. Note that the initial output does

not exhibit such a speckled intensity distributions because the number os modes in the GRIN is orders of magnitude less than the other fibers studied in this work, for example the MMF and MCF.

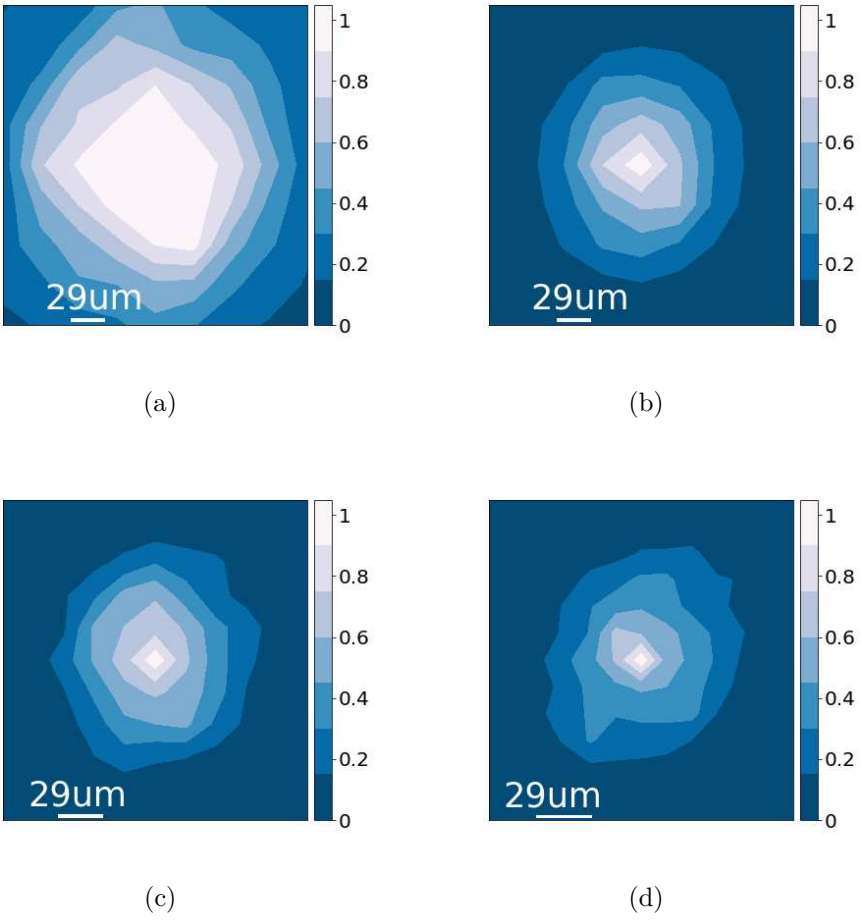

Figure 4.2: Experimental results for focusing with a multimode GRIN fiber: In 4.2a, the initial output intensity distribution. In 4.2b, 4.2c and 4.2d, the focal spots generated with different diameters, through optimized TMs, respectively: 29 μm, 24 μm and 20 μm.

To quantify the stability of the phase masks optimized, the optical contrast of the induced focus was measured through 14 days. These results are shown in Figure 4.3. The optical contrast for the 24 μm-diameter focus was the measurement that varied the most. It was found that only after 7 days, the values of optical contrasts decreased a maximum of 8 % from the initial measurements. Since then, accumulated disturbances caused minor misalignments which impaired focus quality in more than 28 %. after 14 days from the optimization. As for the other focus spots after 14 days, the optical contrasts values suffered only 12 % for the 29 μm, and 20 % for the 20 μm.

Still, it was proved that the optimized TMs can hold satisfactory focus quality after a week for all the focus diameters studied.

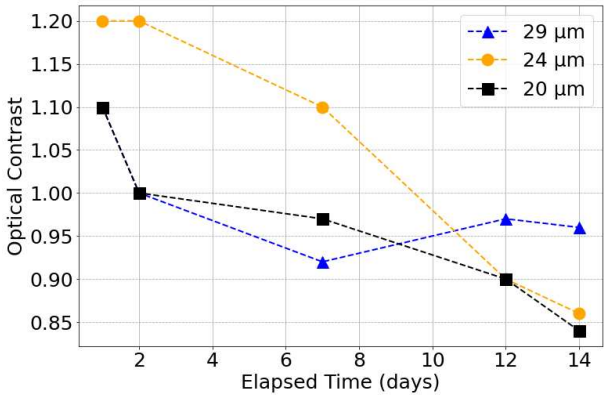

Figure 4.3: Stability of optical contrast measurements for focal diameters of 29 μm, 24 μm and 20 μm.

4.2 Fiber-to-fiber coupling

From the results obtained for focusing with a GRIN fiber, we can assume that is possible keep focus quality for an extended period of time. Therefore, it is no longer required to monitor the distal end of the fiber to check for focus, enabling a myriad of applications, such as free space coupling.

The CCD was then, replaced with a conventional SMF with a 8 μm-core in order to test free space coupling between the two fibers, as shown in Figure 4.4.

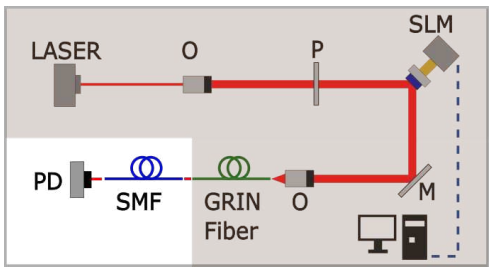

(a)

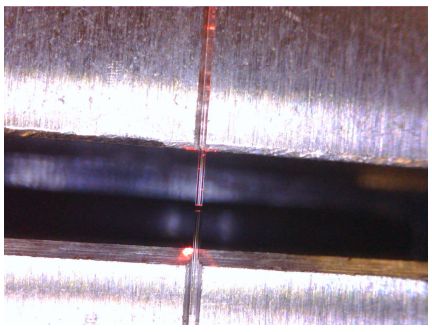

(b)

Figure 4.4: In (a), the scheme of the experimental setup for GRIN and SMF free space coupling. In (b), a picture of the interface between the fibers.

To evaluate coupling, the fibers were aligned and power measurements were taken with and without the optimized phase mask, for the three different focal diameters

earlier studied. To assure better results, the phase masks used for the coupling experiment were brand new so their optical contrast agree with the values presented in Table 4.1.

The power measurements presented are averages of 200 repetitions, so power oscillations, temperature variations, mechanical disturbances and any other noises could be considered. Besides that, the standard deviation for each measure was taken. These values can be seen in Table 4.2.

The results show that inducing focus at the tip of the GRIN fiber can improve fiber to fiber coupling in free space, when comparing to back to back coupling without shaping the wavefronts with the optimized masks. By decreasing the diameters of the focus spot, it is possible to, significantly, enhance the output power. With the 20 μm-diameter focus, an improvement of up to 2.22 dB in coupling was measured. Although for focus spots whose diameters are larger- approximately half the original spot- there are no noticeable enhancement in the output power, as it can be seen for 29 μm-diameter focus.

All the successful focusing experiments performed so far, indicate that modal mixing has been efficient characterized. Thus, we can infer that there is a certain tolerance that focus could still be achieved even with additional modal disruptions, such as spacial displacements of the input fiber.

Aiming to test the suitability of the transmission matrices acquired for this situation, the GRIN fiber was shifted 50 μm in the longitudinal axis and coupling was again experimented. The additional modal interference cause by the displacement reduced the quality of coupling, however, the focus spots studied with smaller diameters (24 µm and 20 µm), a 2 dB gain in the output power was still noticed when comparing to coupling without using the phase masks. For larger focus, there were no advantages in using the phase masks, which shows that the induced modal interference overcame the characterization made. The results that led to this discussion are also presented in Table 4.2.

Table 4.2: GRIN-SMF coupling results.

	Output power enhancement (dB)	
Focus diameter (µm)	Butt-coupled fibers	Fibers 50 µm apart
20	3.47 ± 0.31	3.32 ± 0.16
24	3.23 ± 0.14	2.46 ± 0.01
29	1.19 ± 0.34	0.30 ± 0.41

Analyzing the results according to their coupling efficiency, they better show the advantages of applying the method in coupling experiments. With no wavefront shaping, the coupling efficiency for fiber-to-fiber configuration is only 40%, which means that 60% of the incoming power was lost. When using the optimized phase masks, the efficiency improved to 93%, for the 20 µm focal spot, and 67% for the 29 µm focal spot. When the fibers were moved 50 µm apart, the coupling efficiency without any optimization resulted in only of the incoming power 35% being coupled to the fiber. With the phase masks, it

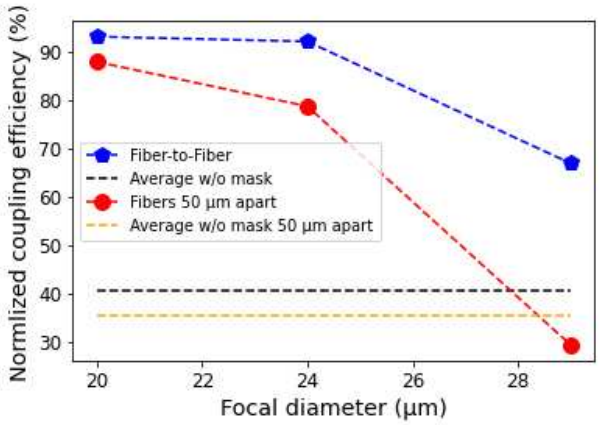

Figure 4.5: Coupling effiency for fiber-to-fiber configuration.

was possible to reach 88% of coupling efficiency. Therefore, the enhancements obtained are very significant and competitive when it comes to other coupling configuration such as using the lensed fiber. The data can be found in Figure 4.5.

4.3 Fiber-to-chip coupling

Still exploring more efficient couplings, a lateral fiber-to-chip coupling was studied. In this configuration, it is also common to use lensed fibers [78]. However, we experiment, in here, how the optimized phase masks can positively contribute with this type of coupling as well.

The experimental setup, was again, adapted. In this case, integrated SU-8 waveguides were fabricated on a silicon dioxide buffer, with air cladding, and were aligned with an input GRIN fiber while their output power was collected with a MMF. The setup is illustrated in Figure 4.6. The width of the waveguides was 50 µm, and two core thicknesses were tested: 50 µm and 127 µm, with two samples for each one.

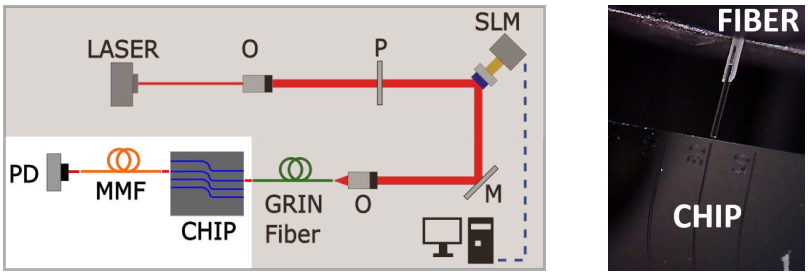

(a) (b)

Figure 4.6: Fiber-to-chip coupling experimental setup. In (a), a diagram of the setup and in (b), a photo of the interface between the GRIN fiber and the waveguide on the silicon dioxide buffer.

In this experiment, we also show that the optimized phase masks depend only

on the characterized waveguide, in this case, the GRIN fiber. This independence was demonstrated by replacing the 633 nm laser source by a super-continuum. It is important to note that the SLM plays a role of wavelength filter, once it operates at the first diffraction order of the 633 nm wavelength. Therefore, the phase masks should still be able to induce focus. To assure that the super-continuum source does not present any significant power variations, the graph in Figure 4.7 shows its quadratic error in magnitude over one hour.

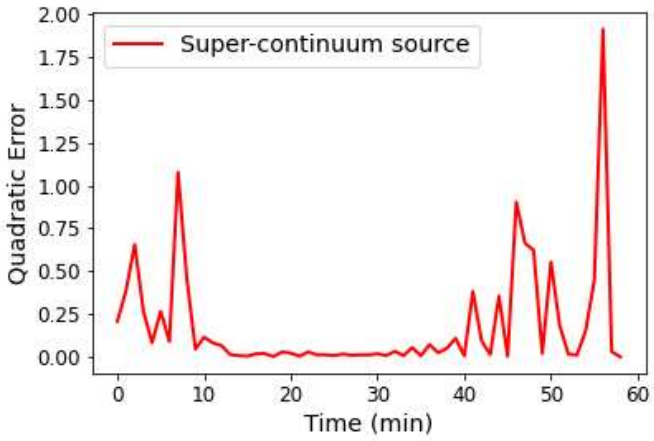

Figure 4.7: Stability measurements with a GRIN fiber, over one hour, with super-continuum source, at the first diffraction order of the 633 nm.

Table 4.3: GRIN fiber-to-chip coupling results. Samples 1 and 2 have core thickness of 50 µm, and samples 3 and 4, of 127 µm.

	Output power enhancement (dB)			
Focus diameter (µm)	Sample 1	Sample 2	Sample 3	Sample 4
20	4.40 ± 0.41	4.77 ± 0.36	4.64 ± 0.50	4.27 ± 0.53
24	3.58 ± 0.43	4.02 ± 0.48	3.88 ± 0.60	3.53 ± 0.50
29	3.25 ± 0.53	3.59 ± 0.48	3.53 ± 0.68	3.02 ± 0.38

The output power measurements collected in the coupling experiments are organized in Table 4.3. Samples 1 and 2 correspond to the waveguide with a 50 µm core, while samples 3 and 4, refer to the 127 µm-core waveguides. These data are also the averages of 200 measurements taken with their respective standard deviation.

From Table 4.3, it is possible to notice that, overall, as focus diameter decreases, the enhancement in the output power of the waveguides, increase.

Although samples 3 and 4 are ticker and less effective focusing is expected on those due to a more complex modal distribution, they still presented satisfactory improvement in their output power, especially for the 20 µm diameter-focus. However, this explain the minor difference in enhancement that these samples had for focus diameters of 24 µm and 29 µm. Still, all samples presented significant improvement in coupling. For a 24.0 µm-focal diameter, an increase of about 4.0 dB can be seen in all waveguides. As the

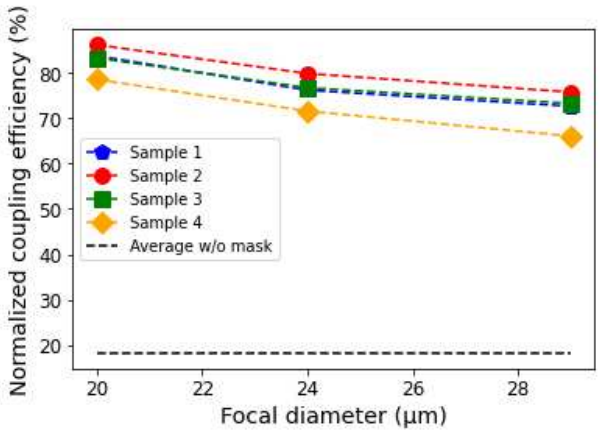

Figure 4.8: Coupling effiency for fiber-to-fiber configuration.

diameter decreases to 20 µm an even more satisfactory enhancement in the order of 4.5 dB was obtained.

The coupling efficiency analysis made for the fiber-to-fiber coupling can be repeated here. The average efficiency for the fiber-to-chip coupling is 18%, which corresponds to a 82% loss. Such value generally disqualifies the experiment, however, by shaping the wavefronts, the coupling efficiency for this experiment also had notable enhancements. It was found that with the phase mask that generate a focal spot with a 20 µm diameter, the efficiency improved to 86% and for the 29 µm-diameter focus, the coupling effiency still showed positive results of approximately 66%. The complete analysis is detailed in Figure 4.8.

These results show that the experimental setup proposed can be expanded to several coupling applications, and can be an asset when dealing with lower optical power. Besides, it eliminates any additional fabrication on the tip of the fiber and can tune its convergence, by adjusting the focal diameter, according to necessity.

4.4 Conclusion

Focusing with a GRIN fiber resulted in direct coupling applications. The first step to perform the coupling experiments was to characterize the modal dispersion of the GRIN fiber by optimizing phase masks for specific focal targets, as it was done for the previous fibers.

The phase masks were satisfactorily obtained with optical contrasts greater than unity. If a comparison is made between these values and the optical contrasts from the MMF and the MCF, it will be noticed that the values for the GRIN fiber are lower. However, this fiber presents a different modal distribution. In reality, there are lesser and more controlled modes in the GRIN fiber, due to its parabolic refractive index which leads to different propagation characteristics [79] from the other fibers, here studied.

A 14 days-analysis of the stability of the optical contrasts obtained for GRIN fiber was done. We can infer that the quality of focus holds even when after several days. Less than 8 % decrease in the optical contrast were measured after a period of 7 days. This analysis supports the hypothesis that the optimized transmission matrix is stable enough, so it is so no longer required to monitor the distal end of the fiber to assure focus quality.

By freeing the distal end of the fiber, the experiment is more suitable for the aimed applications in bio-imaging and integrated systems.

So, we proposed using lensless GRIN fibers in coupling experiments. The first experiment presented a fiber-to-fiber configuration and the second, a fiber-to-chip.

For the fiber-to-fiber coupling, by using the transmission matrices earlier acquired, it was possible to enhance the output power in up to 3.47 dB (93% coupling efficiency) for a 20 µm resolution and in 1.19 dB (67% coupling efficiency), for a 29 µm resolution.

As for the fiber-to-chip, for a 20 µm resolution, coupling efficiency enhanced in, approximately 4.5 dB (83% coupling efficiency) for 50 µm and 127 µm thick-waveguides. For a 29 µm resolution, the enhancement measure was, approximately, 3.3 dB (75% coupling efficiency).

Experimentally measuring enhancement in coupling without the use of any lenses on the tip of the fiber is a relevant conclusion of this work, which aimed contribute to the integrated systems field. Besides, we show that it is possible can tune the resolution desired by optimizing the phases masks accordingly and choose the incoming wavelength.

Chapter 5

Conclusion

The project developed consists on generating focal spots from speckle patterns in different multimode waveguides, using a experimental setup that does not require a reference beam. We proposed imaging experiments that could be feasible to bio-imaging and coupling in integrated systems.

This work began with a review in literature to emphasize the relevance and motivation of imaging with multimode waveguides. Then, studies about obtaining focus from speckle patterns were conducted and are emphasized here:

For a multimode fiber with 61.5 μm core, focusing was achieved for different resolutions at 633 nm. The quality of the images obtained was evaluated according to their optical contrast. All measurements acquired were successful and showed optical contrast greater than 1, which indicates uniform power distribution and clear focal patterns.

Then, aiming to explore the spatial tuning of the focal spot, a multicore fiber was analyzed. Transmission matrices were optimized in order to, individually excite cores. It was found that such measurements are possible since the focal spots obtained at selected cores presented high intensity contrast. Later, a superposition of the phase masks were tested so multiple cores could be illuminated simultaneously. Such experiment also had satisfactory results but only with pairs of cores, as the noise superposition from each individual imaging impairs focusing significantly with more than cores at once.

The study of fiber bundles showed that the method is also efficient to induce focus with disordered gathering of fibers. Fiber bundles with different quantities of fiber cores (approximately, 70 fiber cores and 200 fiber cores) were assembled in the laboratory and focus was acquired for both of them in different spatial positions. These waveguides imposed more difficult challenges in optimizations once the number of modes presented was much larger than from the fibers earlier worked. Still, by adjusting the size of the optimization data base, focus spots were obtained with resolutions of about 130 µm.

Then, attracted by the parabolic refractive index profile of graded index fibers and their smaller amount of modes, focusing experiments were carried out.

By using GRIN fibers as the waveguide, great quality focus and resolutions up

to 20 µm were achieved. It was possible to tune the diameter of the focal spot and the measurements accounted for satisfactory stability throughout days.

This feature makes the monitoring of the distal end of the fiber no longer necessary. So, we proposed coupling experiments using fiber-to-fiber and fiber-to-chip configurations.

GRIN fiber are commonly used for coupling in integrated systems, however, for efficient interfaces, lenses at the tip of the fibers are usually fabricated. In this work, coupling was experimented using the optimized phase mask - only - to generate focus, therefore, we eliminated the necessity to fabricate additional structure on the fibers.

To begin with, fiber-to-fiber coupling was studied with the input GRIN fiber and a SMF. It was found that the output power at the coupling could be enhanced by up to 3.4 dB, approximately. Also, as additional modal mixing could happen during coupling measurements, the input fiber was dislocated a few tens of microns. Even in this situation, the optimized phase mask tolerated such extra interference and still resulted in enhancements at the output power, yet they are slightly less than for the non-displaced setting.

To approach coupling in integrated systems, SU-8 waveguides were fabricated on a silicon buffer with air cladding. Four samples were used for the coupling experiment, each pair with different thickness. Average enhancements of 4 dB were obtained in this configuration.

So, we showed that by applying this method, coupling can be enhanced and simplified once it does not require the fabrication of any structures on the tip of the fiber, as it is commonly done. Due to the degrees of freedom chosen, it is also possible to tune the diameter of the focal spot and the system can account for different wavelengths.

Moreover, the phase masks obtained show great stability, which means that they can be used for periods of time, such as days, without significant impairment in focus quality. Over a week, less than 10% reduction was measured in the contrast.

In conclusion, the proposed experiment is suitable for several practical applications in integrated systems and also in bio-imaging.

5.1 Future Steps

Once focusing was achieved with the multimode fibers studied, imaging with more complex multimode structures is aimed. The future steps of this work consists on fabricating and generating focus with microgrippers [80], and even optical tweezers. Future developments also includes improving the method, so specific modes of the waveguides can be excited.

References

[1] G. P. Agrawal, *Fiber-optic communication systems*, vol. 222. John Wiley & Sons, 2012.

[2] A. Boniface, J. Dong, and S. Gigan, "Non-invasive focusing and imaging in scattering media with a fluorescence-based transmission matrix," *Nature communications*, vol. 11, no. 1, pp. 1–7, 2020.

[3] L. Zhu, F. Soldevila, C. Moretti, A. d'Arco, A. Boniface, X. Shao, H. B. de Aguiar, and S. Gigan, "Large field-of-view non-invasive imaging through scattering layers using fluctuating random illumination," *Nature communications*, vol. 13, no. 1, pp. 1–6, 2022.

[4] H. Ruan, J. Xu, and C. Yang, "Optical information transmission through complex scattering media with optical-channel-based intensity streaming," *Nature Communications*, vol. 12, no. 1, pp. 1–10, 2021.

[5] S. Li, C. Saunders, D. J. Lum, J. Murray-Bruce, V. K. Goyal, T. Čižmár, and D. B. Phillips, "Compressively sampling the optical transmission matrix of a multimode fibre," *Light: Science & Applications*, vol. 10, no. 1, pp. 1–15, 2021.

[6] L. V. Amitonova and J. F. De Boer, "Compressive imaging through a multimode fiber," *Optics letters*, vol. 43, no. 21, pp. 5427–5430, 2018.

[7] T. Zhao, S. Ourselin, T. Vercauteren, and W. Xia, "Seeing through multimode fibers with real-valued intensity transmission matrices," *Optics Express*, vol. 28, no. 14, pp. 20978–20991, 2020.

[8] C. Li, D. Liu, and D. Dai, "Multimode silicon photonics," *Nanophotonics*, vol. 8, no. 2, pp. 227–247, 2019.

[9] D. Malacara, *Optical shop testing*, vol. 59. John Wiley & Sons, 2007.

[10] P. A. Mello, E. Akkermans, and B. Shapiro, "Macroscopic approach to correlations in the electronic transmission and reflection from disordered conductors," *Physical review letters*, vol. 61, no. 4, p. 459, 1988.

[11] C. W. Beenakker, "Random-matrix theory of quantum transport," *Reviews of modern physics*, vol. 69, no. 3, p. 731, 1997.

[12] R. Carminati, J. Saenz, J.-J. Greffet, and M. Nieto-Vesperinas, "Reciprocity, unitarity, and time-reversal symmetry of the s matrix of fields containing evanescent components," *Physical review A*, vol. 62, no. 1, p. 012712, 2000.

[13] L. Borcea, G. Papanicolaou, C. Tsogka, and J. Berryman, "Imaging and time reversal in random media," *Inverse Problems*, vol. 18, no. 5, p. 1247, 2002.

[14] S. Popoff, G. Lerosey, M. Fink, A. C. Boccara, and S. Gigan, "Controlling light through optical disordered media: transmission matrix approach," *New Journal of Physics*, vol. 13, no. 12, p. 123021, 2011.

[15] S. Popoff, G. Lerosey, R. Carminati, M. Fink, A. Boccara, and S. Gigan, "Measuring the transmission matrix in optics: an approach to the study and control of light propagation in disordered media," *Physical review letters*, vol. 104, no. 10, p. 100601, 2010.

[16] S. Popoff, G. Lerosey, M. Fink, A. C. Boccara, and S. Gigan, "Image transmission through an opaque material," *Nature communications*, vol. 1, p. 81, 2010.

[17] P. Zhou, X. Liu, Y. He, and T. Zhu, "Phase error analysis and compensation considering ambient light for phase measuring profilometry," *Optics and Lasers in Engineering*, vol. 55, pp. 99–104, 2014.

[18] I. M. Vellekoop and A. Mosk, "Focusing coherent light through opaque strongly scattering media," *Optics letters*, vol. 32, no. 16, pp. 2309–2311, 2007.

[19] T. Čižmár and K. Dholakia, "Exploiting multimode waveguides for pure fibre-based imaging," *Nature communications*, vol. 3, p. 1027, 2012.

[20] S. Bianchi and R. Di Leonardo, "A multi-mode fiber probe for holographic micromanipulation and microscopy," *Lab on a Chip*, vol. 12, no. 3, pp. 635–639, 2012.

[21] I. Gusachenko, J. Nylk, J. A. Tello, and K. Dholakia, "Multimode fibre based imaging for optically cleared samples," *Biomedical optics express*, vol. 8, no. 11, pp. 5179–5190, 2017.

[22] T. Čižmár and K. Dholakia, "Shaping the light transmission through a multimode optical fibre: complex transformation analysis and applications in biophotonics," *Optics Express*, vol. 19, no. 20, pp. 18871–18884, 2011.

[23] N. Stasio, D. B. Conkey, C. Moser, and D. Psaltis, "Light control in a multicore fiber using the memory effect," *Optics express*, vol. 23, no. 23, pp. 30532–30544, 2015.

[24] R. N. Mahalati, R. Y. Gu, and J. M. Kahn, "Resolution limits for imaging through multi-mode fiber," *Optics express*, vol. 21, no. 2, pp. 1656–1668, 2013.

[25] I. Waldspurger, A. d'Aspremont, and S. Mallat, "Phase recovery, maxcut and complex semidefinite programming," *Mathematical Programming*, vol. 149, no. 1-2, pp. 47–81, 2015.

[26] A. A. Juarez, C. A. Bunge, S. Warm, and K. Petermann, "Perspectives of principal mode transmission in mode-division-multiplex operation," *Optics express*, vol. 20, no. 13, pp. 13810–13824, 2012.

[27] A. Trichili, K.-H. Park, M. Zghal, B. S. Ooi, and M.-S. Alouini, "Communicating using spatial mode multiplexing: potentials, challenges, and perspectives," *IEEE Communications Surveys & Tutorials*, vol. 21, no. 4, pp. 3175–3203, 2019.

[28] B. Stern, X. Zhu, C. P. Chen, L. D. Tzuang, J. Cardenas, K. Bergman, and M. Lipson, "On-chip mode-division multiplexing switch," *Optica*, vol. 2, no. 6, pp. 530–535, 2015.

[29] S. Berdagué and P. Facq, "Mode division multiplexing in optical fibers," *Applied optics*, vol. 21, no. 11, pp. 1950–1955, 1982.

[30] M. Plöschner, T. Tyc, and T. Čižmár, "Seeing through chaos in multimode fibres," *Nature Photonics*, vol. 9, no. 8, p. 529, 2015.

[31] G. S. Gordon, R. Mouthaan, T. D. Wilkinson, and S. E. Bohndiek, "Coherent imaging through multicore fibres with applications in endoscopy," *Journal of Lightwave Technology*, vol. 37, no. 22, pp. 5733–5745, 2019.

[32] R. Ma, Y. J. Rao, W. L. Zhang, and B. Hu, "Multimode random fiber laser for speckle-free imaging," *IEEE Journal of Selected Topics in Quantum Electronics*, vol. 25, no. 1, pp. 1–6, 2018.

[33] X. Hu, J. Zhao, J. E. Antonio-Lopez, S. Fan, R. A. Correa, and A. Schülzgen, "Robust imaging-free object recognition through anderson localizing optical fiber," *Journal of Lightwave Technology*, vol. 39, no. 4, pp. 920–926, 2021.

[34] S. Silva, E. G. Pachon, M. A. Franco, P. Jorge, J. Santos, F. X. Malcata, C. M. Cordeiro, and O. Frazão, "Curvature and temperature discrimination using multimode interference fiber optic structures—a proof of concept," *Journal of Lightwave technology*, vol. 30, no. 23, pp. 3569–3575, 2012.

[35] D. Loterie, S. Farahi, I. Papadopoulos, A. Goy, D. Psaltis, and C. Moser, "Digital confocal microscopy through a multimode fiber," *Optics express*, vol. 23, no. 18, pp. 23845–23858, 2015.

[36] E. Auksorius, D. Borycki, and M. Wojtkowski, "Multimode fiber enables control of spatial coherence in fourier-domain full-field optical coherence tomography for in vivo corneal imaging," *Optics Letters*, vol. 46, no. 6, pp. 1413–1416, 2021.

[37] M. Plöschner, V. Kollárová, Z. Dostál, J. Nylk, T. Barton-Owen, D. E. Ferrier, R. Chmelík, K. Dholakia, and T. Čižmár, "Multimode fibre: Light-sheet microscopy at the tip of a needle," *Scientific reports*, vol. 5, no. 1, pp. 1–7, 2015.

[38] T. M. Urner, A. Inman, B. Lapid, and S. Jia, "Three-dimensional light-field microendoscopy with a grin lens array," *Biomedical Optics Express*, vol. 13, no. 2, pp. 590–607, 2022.

[39] A. M. Caravaca-Aguirre and R. Piestun, "Single multimode fiber endoscope," *Optics express*, vol. 25, no. 3, pp. 1656–1665, 2017.

[40] Z. Ju, Z. Yu, Z. Meng, N. Zhan, L. Gui, and K. Xu, "Simultaneous illumination and imaging based on a single multimode fiber," *Optics Express*, vol. 30, no. 9, pp. 15596–15606, 2022.

[41] B. Rahmani, I. Oguz, U. Tegin, J.-l. Hsieh, D. Psaltis, and C. Moser, "Learning to image and compute with multimode optical fibers," *Nanophotonics*, vol. 11, no. 6, pp. 1071–1082, 2022.

[42] L. Wu, J. Zhao, M. Zhang, Y. Zhang, X. Wang, Z. Chen, and J. Pu, "Deep learning: High-quality imaging through multicore fiber," *Current Optics and Photonics*, vol. 4, no. 4, pp. 286–292, 2020.

[43] W. Klaus, J. Sakaguchi, B. J. Puttnam, Y. Awaji, N. Wada, T. Kobayashi, and M. Watanabe, "Free-space coupling optics for multicore fibers," *IEEE Photonics Technology Letters*, vol. 24, no. 21, pp. 1902–1905, 2012.

[44] K. Saitoh and S. Matsuo, "Multicore fiber technology," *Journal of Lightwave Technology*, vol. 34, no. 1, pp. 55–66, 2016.

[45] S. S. Azadeh, A. Stalmashonak, K. W. Bennett, F.-D. Chen, W. D. Sacher, and J. K. Poon, "Multicore fibers with 10 and 16 single-mode cores for the visible spectrum," *Optics letters*, vol. 47, no. 1, pp. 26–29, 2022.

[46] R. Ryf, N. K. Fontaine, H. Chen, B. Guan, B. Huang, M. Esmaeelpour, A. Gnauck, S. Randel, S. Yoo, A. Koonen, *et al.*, "Mode-multiplexed transmission over conventional graded-index multimode fibers," *Optics express*, vol. 23, no. 1, pp. 235–246, 2015.

[47] W. H. Renninger and F. W. Wise, "Optical solitons in graded-index multimode fibres," *Nature communications*, vol. 4, no. 1, pp. 1–6, 2013.

[48] T. Hansson, A. Tonello, T. Mansuryan, F. Mangini, M. Zitelli, M. Ferraro, A. Niang, R. Crescenzi, S. Wabnitz, and V. Couderc, "Nonlinear beam self-imaging and self-focusing dynamics in a grin multimode optical fiber: theory and experiments," *Optics Express*, vol. 28, no. 16, pp. 24005–24021, 2020.

[49] G. P. Agrawal, "Invite paper: Self-imaging in multimode graded-index fibers and its impact on the nonlinear phenomena," *Optical Fiber Technology*, vol. 50, pp. 309–316, 2019.

[50] W. Wang, J. Ma, and B.-O. Guan, "Truncated conical-tip fiber probe for common-path optical coherence tomography with optimal sensitivity," *Journal of Lightwave Technology*, 2022.

[51] X. Sun, K. Bedard, and J. Li, "Optical fiber probe for optical coherence tomography with extended depth of field using a modified grin fiber lens," in *Optical Fibers and Sensors for Medical Diagnostics, Treatment and Environmental Applications XXII*, vol. 11953, pp. 44–49, SPIE, 2022.

[52] W. Zong, H. A. Obenhaus, E. R. Skytøen, H. Eneqvist, N. L. de Jong, R. Vale, M. R. Jorge, M.-B. Moser, and E. I. Moser, "Large-scale two-photon calcium imaging in freely moving mice," *Cell*, vol. 185, no. 7, pp. 1240–1256, 2022.

[53] J. D. Rees, "Non-gaussian imaging properties of grin fiber lens arrays," *Applied Optics*, vol. 21, no. 6, pp. 1009–1012, 1982.

[54] E. Swanson, C. L. Petersen, E. McNamara, R. B. Lamport, and D. L. Kelly, "Ultra-small optical probes, imaging optics, and methods for using same," Sept. 3 2002. US Patent 6,445,939.

[55] Y. Mao, S. Chang, S. Sherif, and C. Flueraru, "Graded-index fiber lens proposed for ultrasmall probes used in biomedical imaging," *Applied optics*, vol. 46, no. 23, pp. 5887–5894, 2007.

[56] D. Lorenser, X. Yang, and D. D. Sampson, "Ultrathin fiber probes with extended depth of focus for optical coherence tomography," *Opt. Lett.*, vol. 37, pp. 1616–1618, May 2012.

[57] Y.-F. Chien, J.-Y. Lin, P.-T. Yeh, K.-J. Hsu, Y.-H. Tsai, S.-K. Chen, and S.-W. Chu, "Dual grin lens two-photon endoscopy for high-speed volumetric and deep brain imaging," *Biomed. Opt. Express*, vol. 12, pp. 162–172, Jan 2021.

[58] N. Riesen, N. Phillips, L. V. Nguyen, S. C. Warren-Smith, C. Priest, and D. G. Lancaster, "Design considerations for graded index fiber tip fabry–perot interferometers," *Measurement Science and Technology*, vol. 32, no. 5, p. 055201, 2021.

[59] W. Song, Y. Xie, Z. Li, W. Hao, P. Yan, and X. Li, "Single-mode fiber to grin-rod lenses coupling efficiency and tolerance analysis," in *Global Intelligent Industry Conference 2020*, vol. 11780, p. 117801E, International Society for Optics and Photonics, 2021.

[60] M. Zickar, W. Noell, C. Marxer, and N. de Rooij, "Mems compatible micro-grin lenses for fiber to chip coupling of light," *Opt. Express*, vol. 14, pp. 4237–4249, May 2006.

[61] Q. Wang, Y. Huang, T.-H. Loh, D. K. T. Ng, and S.-T. Ho, "Thin-film stack based integrated grin coupler with aberration-free focusing and super-high na for efficient fiber-to-nanophotonic-chip coupling," *Opt. Express*, vol. 18, pp. 4574–4589, Mar 2010.

[62] Y. Hwang, N. Phillips, D. E. Otten, N. Riesen, and D. G. Lancaster, "Efficient coupling between single mode fibers and glass chip waveguides via graded refractive index fiber tips," *Optics Express*, vol. 30, no. 8, pp. 12294–12307, 2022.

[63] I. N. Papadopoulos, S. Farahi, C. Moser, and D. Psaltis, "Focusing and scanning light through a multimode optical fiber using digital phase conjugation," *Optics express*, vol. 20, no. 10, pp. 10583–10590, 2012.

[64] H. Yu, T. R. Hillman, W. Choi, J. O. Lee, M. S. Feld, R. R. Dasari, and Y. Park, "Measuring large optical transmission matrices of disordered media," *Physical review letters*, vol. 111, no. 15, p. 153902, 2013.

[65] M. N'Gom, T. B. Norris, E. Michielssen, and R. R. Nadakuditi, "Mode control in a multimode fiber through acquiring its transmission matrix from a reference-less optical system," *Optics letters*, vol. 43, no. 3, pp. 419–422, 2018.

[66] M. N'Gom, M.-B. Lien, N. M. Estakhri, T. B. Norris, E. Michielssen, and R. R. Nadakuditi, "Controlling light transmission through highly scattering media using semi-definite programming as a phase retrieval computation method," *Scientific reports*, vol. 7, no. 1, p. 2518, 2017.

[67] J. H. Song, H. N. Fernando, B. Roycroft, B. Corbett, and F. H. Peters, "Practical design of lensed fibers for semiconductor laser packaging using laser welding technique," *Journal of lightwave technology*, vol. 27, no. 11, pp. 1533–1539, 2009.

[68] K. Okamoto, *Fundamentals of optical waveguides*. Elsevier, 2021.

[69] Y.-Y. Xie, B.-Y. Wang, Z.-J. Cheng, Q.-Y. Yue, and C.-S. Guo, "Measurement of vector transmission matrix and control of beam focusing through a multiple-scattering medium based on a vector spatial light modulator and two-channel polarization holography," *Applied Physics Letters*, vol. 110, no. 22, p. 221105, 2017.

[70] J. Xu, H. Ruan, Y. Liu, H. Zhou, and C. Yang, "Focusing light through scattering media by transmission matrix inversion," *Optics express*, vol. 25, no. 22, pp. 27234–27246, 2017.

[71] R. W. Gerchberg, "A practical algorithm for the determination of phase from image and diffraction plane pictures," *Optik*, vol. 35, pp. 237–246, 1972.

[72] A. Apostol and A. Dogariu, "Non-gaussian statistics of optical near-fields," *Physical Review E*, vol. 72, no. 2, p. 025602, 2005.

[73] A. Farré, M. Shayegan, C. López-Quesada, G. A. Blab, M. Montes-Usategui, N. R. Forde, and E. Martín-Badosa, "Positional stability of holographic optical traps," *Optics express*, vol. 19, no. 22, pp. 21370–21384, 2011.

[74] A. Lizana, I. Moreno, A. Márquez, C. Iemmi, E. Fernández, J. Campos, and M. Yzuel, "Time fluctuations of the phase modulation in a liquid crystal on silicon display: characterization and effects in diffractive optics," *Optics express*, vol. 16, no. 21, pp. 16711–16722, 2008.

[75] A. Bergeron, J. Gauvin, F. Gagnon, D. Gingras, H. H. Arsenault, and M. Doucet, "Phase calibration and applications of a liquid-crystal spatial light modulator," *Applied optics*, vol. 34, no. 23, pp. 5133–5139, 1995.

[76] S. S. Azadeh, A. Stalmashonak, K. W. Bennett, F.-D. Chen, W. D. Sacher, and J. K. S. Poon, "Multicore fibers with 10 and 16 single-mode cores for the visible spectrum," *Opt. Lett.*, vol. 47, pp. 26–29, Jan 2022.

[77] F. Beltrán-Mejía, C. R. Biazoli, and C. M. Cordeiro, "Tapered grin fiber microsensor," *Optics Express*, vol. 22, no. 25, pp. 30432–30441, 2014.

[78] V. R. Almeida, R. R. Panepucci, and M. Lipson, "Nanotaper for Compact Mode Conversion," *Optics Letters*, vol. 28, p. 1302, Aug. 2003.

[79] L. Jacomme, "Modal dispersion in multimode graded-index fibers," *Applied optics*, vol. 14, no. 11, pp. 2578–2584, 1975.

[80] R. R. Panepucci and J. A. Martinez, "Novel su-8 optical waveguide microgripper for simultaneous micromanipulation and optical detection," *Journal of Vacuum Science & Technology B: Microelectronics and Nanometer Structures Processing, Measurement, and Phenomena*, vol. 26, no. 6, pp. 2624–2627, 2008.